AMERICAN METEOROLOGICAL SOCIETY

Journal of Physical Oceanography

EARLY ONLINE RELEASE

This is a preliminary PDF of the author-produced manuscript that has been peer-reviewed and accepted for publication. Since it is being posted so soon after acceptance, it has not yet been copyedited, formatted, or processed by AMS Publications. This preliminary version of the manuscript may be downloaded, distributed, and cited, but please be aware that there will be visual differences and possibly some content differences between this version and the final published version.

The DOI for this manuscript is doi: 10.1175/JPO-D-18-0161.1

The final published version of this manuscript will replace the preliminary version at the above DOI once it is available.

If you would like to cite this EOR in a separate work, please use the following full citation:

Williams, D., K. Horsburgh, D. Schultz, and C. Hughes, 2018: Examination of generation mechanisms for an English Channel meteotsunami: combining observations and modeling. J. Phys. Oceanogr. doi:10.1175/JPO-D-18-0161.1, in press.

© 2018 American Meteorological Society

LaTeX File (.tex, .sty, .cls, .bst, .bib)
Click here to access/download;LaTeX File (.tex, .sty, .cls, .bst, .bib);Williamsetal2018_Revisions.tex

Examination of generation mechanisms for an English Channel meteotsunami: combining observations and modeling

David A Williams*

Department of Earth, Ocean and Ecological Sciences, University of Liverpool, L3 5TR, Liverpool, United Kingdom

Kevin J Horsburgh

National Oceanography Centre Liverpool, L3 5DA, Liverpool, United Kingdom

David M Schultz

School of Earth and Environmental Sciences, University of Manchester, M13 9PL, United Kingdom

Chris W Hughes

Department of Earth, Ocean and Ecological Sciences, University of Liverpool, L3 5TR, Liverpool, United Kingdom

Corresponding author address: Department of Earth, Ocean and Ecological Sciences, University of Liverpool, L3 5TR, Liverpool, United Kingdom

E-mail: David.Williams2@liverpool.ac.uk

PRELIMINARY ACCEPTED VERSION

ABSTRACT

On the morning of 23 June 2016, a 0.70 m meteotsunami was observed in the English Channel between the UK and France. This wave was measured by several tide gages and coincided with a heavily precipitating convective system producing 10 m s^{-1} wind speeds at the 10-m level and 1–2.5 hPa surface pressure anomalies. A combination of precipitation rate cross-correlations and NCEP/NCAR Reanalysis 1 data showed that the convective system moved northeastward at 19 ± 2 m s^{-1}. To model the meteotsunami, the finite element model Telemac was forced with an ensemble of prescribed pressure forcings, covering observational uncertainty. Ensembles simulated the observed wave period and arrival times within minutes, and wave heights within tens of centimeters. A directly forced wave and a secondary coastal wave were simulated, and these amplified as they propagated. Proudman resonance was responsible for the wave amplification, and the coastal wave resulted from strong refraction of the primary wave. The main generating mechanism was the atmospheric pressure anomaly with wind stress playing a secondary role, increasing the first wave peak by 16% on average. Certain tidal conditions reduced modeled wave heights by up to 56%, by shifting the location where Proudman resonance occurred. This shift was mainly from tidal currents, rather than tidal elevation directly affecting shallow water wave speed. An improved understanding of meteotsunami return periods and generation mechanisms would be aided by tide gage measurements sampled at less than 15-minute intervals.

1. Introduction

On the morning of 23 June 2016, a 0.70 m high, 35-minute period wave coinciding with convective storms was observed in the English Channel (Figure 1). This study shows this wave to be a meteorologically generated tsunami, also known as a meteotsunami.

Meteotsunamis are atmospherically generated shallow-water waves in the tsunami frequency band, with periods between 2 minutes and 2 hours (Monserrat et al. 2006). Meteotsunami wave heights are on the order of 0.1–1 m (Monserrat et al. 2006). Meteotsunamis have sporadically occurred in water bodies on every continent (except Antarctica, where there is absence of evidence). In specific locations, such as Nagasaki Bay in Japan (Hibiya and Kajiura 1982), Ciutadella Harbor in Menorca (Rabinovich and Monserrat 1998) or Split in Croatia (Šepić et al. 2012), meteotsunamis repeatedly occur and can reach up to 6 m. They are also recurrent in the Laurentian Great Lakes (Bechle et al. 2016), where strong rip currents are particularly dangerous (Anderson et al. 2015; Linares and Bechle 2018). They have caused substantial economic losses, for example, a 6 m meteotsunami produced $7 million USD of damages in Vela Luka Bay, 1978 (Vučetić et al. 2009). Furthermore, they may cause injury (Sibley et al. 2016), and sometimes fatalities (Monserrat et al. 2006; Linares and Bechle 2018).

In the UK, there have been recorded meteotsunamis along the south coast in 2011 (Tappin et al. 2013) and along the east coast in 2008 and 2015 (Sibley et al. 2016). Although they are seldom reported, damage to boats has been associated with possible meteotsunamis (Haslett et al. 2009). Also, in 2015, a confirmed meteotsunami in Scotland was related to at least one serious injury (Sibley et al. 2016) and, in 1929, suspected meteotsunami was related to two deaths along the UK southern coastline (Haslett et al. 2009). In 2017, a large tsunami-like wave was noticed at high

tide in the Netherlands and was reported by televised weather reports as a meteotsunami generated by a passing convective system.

However, understanding meteotsunami generation around the UK, and in wider European seas, remains poor because these reports lack quantitative generation mechanism explanations. To date, there is no study in this region that relates the observed waves to their meteorological initiation and amplification. That is the motivation for this work. We use combined observations and numerical modeling to quantitatively understand the generation mechanisms, the relative role of atmospheric pressure and wind stress, and the wave amplification.

Meteotsunamis are initiated by pressure and wind stress from moving atmospheric weather systems (Monserrat et al. 2006). Typically, meteotsunami-generating atmospheric systems are hundreds of kilometers in scale and last a few hours — they are mesoscale systems. Since the atmospheric pressure perturbations ($\sim \pm$ 1 hPa) and 10-m wind speeds ($\sim$ 10 m s^{-1}) in mesoscale systems typically produce centimeter-scale sea-surface perturbations, amplification mechanisms are required for large meteotsunamis (Monserrat et al. 2006). This requirement for wave amplification makes meteotsunamis different to storm surges, which are generated over larger time and space scales by cyclones with deep pressure lows ($>$ 50 hPa lower than background pressure) and strong 10-m wind speeds ($>$ 20 m s^{-1}).

Amplification up to an order of magnitude can be provided by resonance between the meteotsunami and atmospheric forcing (external resonance) (Monserrat et al. 2006). Greenspan resonance and Proudman resonance are two candidate external resonances. Greenspan resonance occurs when the atmospheric forcing speed along the coastline is the same as a coastally-trapped edge wave (Greenspan 1956), whereas Proudman resonance occurs when the atmospheric forcing speed is the same as the shallow-water wave speed (Proudman 1929). Numerical models have provided evidence supporting Greenspan resonance in the Great Lakes (Ewing et al. 1954; Anderson

et al. 2015) and Proudman resonance in Adriatic (Šepić et al. 2015), Balearic (Ličer et al. 2017) and East China Sea (Hibiya and Kajiura 1982). Frère et al. (2014) and Tappin et al. (2013) have suggested that Proudman resonance was responsible for observed meteotsunamis around the UK but this has never been demonstrated through numerical modeling, as we do here.

Acquiring evidence for meteotsunami mechanisms away from coastal tide gages is difficult but can be achieved with a dense oceanographic observational network (Sheremet et al. 2016); unfortunately, no such network is in the English Channel. Therefore, we use numerical models for evidence of external resonance. Our approach is to prescribe an analytic atmospheric forcing, guided by observations, to force a hydrodynamic ocean model. We refer to this as a synthetic model, following Ličer et al. (2017). There are two advantages to synthetic models over models forced by numerical weather prediction output (NWP models), despite NWP models' capability for more detailed forcing. Firstly, synthetic models are simpler than NWP models and simulate comparable wave heights and arrival times (Anderson et al. 2015). Secondly, synthetic models allow full control in sensitivity studies when investigating the relative importance of generation mechanisms such as wind stress and pressure disturbances (Bechle and Wu 2014; Anderson et al. 2015; Šepić et al. 2015). For instance, in Lake Erie, wind stress accounts for 30–60% of wave height (Anderson et al. 2015); whereas in the Adriatic, pressure accounts for 90% of wave height (Šepić et al. 2015).

Meteotsunamis may undergo further amplification when approaching coastlines. Basin bathymetry and the coastline shape (referred to in combination as 'geomorphology') amplify meteotsunamis through refraction and shoaling (Levin and Nosov 2009). Simple calculations (Green's Law) suggest that geomorphology in the English Channel amplifies waves by less than an order of magnitude. In this study, we examine amplification due to both external resonance and geomorphology. Because the English Channel is macrotidal ($>$ 4 m tidal range), we also consider

the sensitivity of meteotsunami growth to tides. In South Korea, another macrotidal basin, modeled wave heights change by up to 11% from tidal elevation affecting Proudman resonance, and change by 9% from tidal currents causing refraction (Choi et al. 2014). Therefore, tides may affect wave growth as much as atmospheric forcing.

This paper presents the observations of the 23 June 2016 meteotsunami in the English Channel and shows, with the help of a prescribed analytic atmospheric forcing, the relative importance of the pressure field versus the wind field, external resonance in the meteotsunami generation, the sensitivity in simulations of external resonance to observational uncertainties, and the sensitivity of wave heights to tides. Progress towards operational hazard warning systems for meteotsunamis, as is being worked on in the Adriatic (Vilibić et al. 2016), requires improved regional understanding of meteotsunami generation. We present and analyze oceanographic and atmospheric observations in Section 2, and then present numerical modeling in Section 3. Section 4 concludes and gives recommendations for future work.

2. Observations

a. Sea surface observations

The tide gage locations are shown in Figure 1, and 23 June 2016 water-level time series are shown in Figure 2. The tidal records show that the English Channel is macrotidal, with tidal ranges of 7–8 m near France and 5 m near the UK. The sea level signal was high-pass filtered to isolate the high frequency disturbances. After removing periods greater than 2 hours, the largest residual wave height (peak to trough, red boxes in Figure 2) measured at Boulogne was 0.78 m, and at Dieppe was 0.42 m (BL and DP in Figure 1). No significant residual was measured at Le Havre (LH, Figure 1). Data was missing from 0527–0534 UTC each day at French tide gage

stations (Figure 2), and 0048–0149 UTC at Le Havre, but this did not impede analysis of wave characteristics.

The 1-minute sampled French radar tide gages also showed that the dominant period of this perturbation was 30–35 minutes (Figure 2), within accepted tsunami-period limits (Monserrat et al. 2006). This dominant tsunami signal, isolated with a 10–60 minute period bandpass filter, had similar wave heights to the non-tidal sea-level residual - 0.70 m at Boulogne, and 0.43 m at Dieppe. We took these values as representative wave heights and were deemed large enough to be a meteotsunami (Monserrat et al. 2006). We defined the arrival time as the time at which the residual water level was half of the first peak (which may not be the maximum residual water level), and directly preceded the first peak. The arrival times were 0447 UTC at Boulogne and 0358 UTC at Dieppe, near mid-tide in France (Figure 2). The Newhaven tide gage (NH, Figure 1) suggested that a 0.26 m high wave arrived later, at 0608 $\pm$ 0007 UTC. However, due to the 15-minute data at Newhaven, there was high uncertainty in wave height and arrival time at this location.

b. Atmospheric observations

Convective storms and heavy precipitation were reported across western Europe between 22–23 June 2016. Figure 3 shows 1-km gridded composite radar-derived precipitation rates over the English Channel at (a) 0220 UTC, (b) 0320 UTC and (c) 0440 UTC. A small stratiform-trailing convective storm was embedded in light precipitation (< 5 mm h^{-1}), moving northeastward over the English Channel.

In the following section, the atmospheric properties of this convective system are quantified, and its potential for meteotsunami generation is analyzed. The important atmospheric properties for wave initiation are wind stress and pressure perturbation amplitude.

1) Pressure perturbations and wind stress

To analyze the convective system pressure perturbations, the total measured pressure was high-pass filtered. Figure 4a shows that the maximum pressure perturbations were generally between $\pm$1.5 hPa. As the convective system progressed northeastward (compare Figure 4 and Figure 3), the high pressure anomaly (mesohigh) strengthened, with low pressure anomalies (mesolows) forming ahead of (pre-squall low) and behind (wake low) the mesohigh. The pressure anomalies farther inland, between Evreux-Huest, Pointoise-Aero, Creil, Roissy, Beauvais-Tille, Amieres Glisy, Meaulte, and Merville-Calonne (see locations at Figure 1), also show a pre-squall low and mesohigh progressing northeastward. Figure 3d shows the interpretation of the convective system at 0320 UTC, guided by the low–high–low pressure pattern described in Markowski and Richardson (2011).

Figure 4b shows that at Le Touquet, Boulogne and Calais, moderate winds were measured between the pre-squall low and the mesohigh, interpreted as the gust front. At Le Touquet and Dunkirk, there were also peak winds between the wake low and mesohigh. At Le Touquet, the maximum 10-m wind speed measured prior to the mesohigh were 8 m s^{-1}, and reached a maximum of 10 m s^{-1} after the mesohigh. The Greenwich Lightship buoy (BUOY in Figure 1) also showed a +1.3 hPa high pressure anomaly and 11 m s^{-1} 14-m wind speeds between 0300–0400 UTC (sampled once per hour), broadly agreeing with in-situ land station observations.

2) Convective system velocity

By assuming equilibrium between hydrostatic and atmospheric forces (for example, inverted barometer), calculations suggest that this atmospheric forcing would have only produced a 0.04 m high wave. Therefore, if the observed wave (0.70 m) were produced by this convective system, it would have needed amplification mechanisms. This may have happened if the speed of the

atmospheric system moved at resonant speed. To determine whether external resonance could have occurred, first we calculated the speed of the convective system using two-dimensional cross-correlation of radar-derived precipitation.

Two-dimensional cross-correlation has been previously used to estimate meteotsunami forcing velocity with satellite images of cloud tops (Belušić and Mahović 2009) and radar reflectivity (Wertman et al. 2014). Here, cross-correlation was used on the radar-derived precipitation fields, which should have provided more representative velocities compared to cloud tops. We took the displacement required for the maximum cross-correlation to calculate the velocity of the convective system between time steps. Following Wertman et al. (2014), multiple time steps were used (5, 10, 15, 20 and 30 minutes) between 0200–0400 UTC. However, precautions were taken to remove effects of individual cells. Here, a binary signal was created, equalling 1 when precipitation-rate was greater than a rain-rate threshold and 0 when the rate was less than the threshold. A range of time-steps and thresholds on the two-dimensional cross-correlation allowed analysis of convective system velocity to chosen parameters, and the best range of parameters to be chosen.

When calculating convective system velocity, we assumed straight line motion. With 10-minute time steps and a 15 mm h^{-1} threshold, the convective system velocity was estimated as 19 ± 2 m s^{-1} (all errors here given to 1σ) at a bearing of $035^\circ \pm 3^\circ$. The speed decreased with larger time steps, from 20 ± 2 m s^{-1} at 5 minute time steps to 18 ± 1 m s^{-1} at 20 minute time steps. The system's direction of movement was more poorly defined, changing from $021^\circ \pm 4^\circ$ (more northward) to $047^\circ \pm 8^\circ$ (more eastward) between 5–20 minute time steps. Nevertheless, the speed remained consistently between 17–22 m s^{-1}.

The cross-correlation results were related to the movement of the whole convective system and individual storm cells. Figure 3 shows that three individual gust fronts were identified as the convective system propagated. We identified the gust front as the leading edge of precipitation, which

coincided with higher 10-m wind observations. New gust fronts were identified when a new line of cells were generated ahead of, and disconnected from, previous gust fronts. A gust front that generated new convective cells was a form of discrete propagation and produced unreasonably large velocities at certain time steps, which were subsequently removed. More northward velocities were produced at shorter time steps and higher thresholds, and explained by storm cell motion that was more northward than the convective system motion (Figure 3d). This was because individual cells were shorter-lived, and produced more intense precipitation than the convective system. Multiple analyses of convective system components were necessary to correctly interpret cross-correlation velocities.

To check that the two-dimensional cross-correlation velocity estimates were reasonable, the average 500-hPa wind velocity from NCEP/NCAR Reanalysis 1 (Kalnay et al. 1996) was calculated between 2.5°W–2.5°E, 47.5°N–52.5°N at 0600 UTC. The 500-hPa wind speed is correlated to meteotsunami generation (Vilibić and Šepić 2017) and the speed of convective systems are often near the mid-tropospheric wind speed (Markowski and Richardson 2011). The reanalysis data showed 22 ± 2 m s^{-1} and northeastward ($040° \pm 1°$) wind velocities. Taking into account both the longer, 20 minute time step cross-correlation analysis at 15 mm h^{-1} cut-offs and the NCEP reanalysis wind speed, the system velocity was about 19 m s^{-1} at a bearing of 045°.

c. Analysis of observations

Given a forcing speed, possible external resonance mechanisms were examined. When the Froude number (Fr, atmospheric forcing speed divided by wave speed) was between 0.9–1.1, we considered that external resonance was possible (Vilibić 2008). We used the edge wave speed c_{edge} to determine Greenspan resonance possibility (Greenspan 1956). The edge wave speed of a tsunami-period wave on a constant slope is:

$$c_{edge} = \frac{gT_{wave}}{2\pi} \tan\big(\beta(2n+1)\big), \tag{1}$$

where g is gravitational acceleration (9.81 m s^{-2}), T_{wave} is wave period, β is bathymetric slope, and n is edge wave mode (corresponding to the number of times the trapped edge wave crosses the still water level in the cross-propagation direction).

Taking transects from near Dieppe across the Channel, the bathymetry was approximated by two slopes. The first slope was steeper, decreasing by 21 m between 0–6 km from the coastline ($\beta \approx 0.0035$). The second slope was shallower, decreasing by 20 m between 6–60 km from the coastline ($\beta \approx 0.0004$). This change in gradient is evident when comparing the 20 m and 40 m contours near Dieppe (Figure 1). From Equation 1 and the observed wave period, the edge wave speed was 1.3 m s^{-1} on the shallow slope and 11.6 m s^{-1} on the steep slope. These edge wave speeds were more than 10% slower than the alongshore forcing speed, meaning that Greenspan resonance was not possible.

Next, we investigated Proudman resonance. Proudman resonance occurs when the atmospheric system speed U is near the shallow-water wave speed c (Proudman 1929). The shallow-water wave speed is proportional to water depth H, and is given by:

$$c = \sqrt{gH}. \tag{2}$$

Using a forcing speed of $U = 19$ m s^{-1} and depths at mean sea level (Figure 1), a Froude number between 0.9–1.1 was calculated in the location of the precipitation at 0320 UTC (Figure 3). Therefore, Proudman resonance was possible. This result was also retained when accounting for tides. Assuming that the shallow water wave speed changes with tidal elevation (H_T) and ocean

currents in the wave propagation direction (V_T) (Choi et al. 2014), the shallow water wave speed is approximately:

$$c \approx \sqrt{g\left(H + H_T\right)} + V_T. \tag{3}$$

Including tidal elevation and currents estimates (H_T = –0.5 m, V_T = –1 m s^{-1}) showed that Proudman resonance was possible, but the Proudman resonant region would have moved away from the coastline (compare regions in Figure 1).

We then analyzed expected wave growth under Proudman resonance. Churchill et al. (1995) derive the following relationship for a linear shallow-water wave, η, trapped underneath a constant amplitude, moving forcing assuming one-dimensional, frictionless propagation without planetary rotation:

$$\eta = \frac{x}{2\rho g}\left(-\frac{\partial p}{\partial x} + \frac{\tau_s}{H_{Pr}} \right), \tag{4}$$

where x is distance in the propagation direction, ρ is water density, p is atmospheric pressure, τ_s is surface wind stress, and H_{Pr} is the depth that Fr is 1. If a sea surface perturbation were amplified by Proudman resonance, it would have grown linearly with distance and been a linear combination of the pressure and wind stress forcing. Simply, the sea surface perturbation would have been the combined pressure induced perturbation η_p and wind stress induced perturbation η_τ:

$$\eta = \eta_p + \eta_\tau. \tag{5}$$

For a pressure field approximated by an advecting sinusoid, with maximum pressure change Δp and wavelength λ, the maximum pressure induced perturbation is:

$$\eta_p = \pi \frac{\Delta p}{\rho g} \frac{x}{\lambda}, \tag{6}$$

and using approximations from observations, a 40 km wavelength, 200 Pa pressure perturbation, would have produced a wave height of 0.31 m after moving 200 km across the English Channel towards Boulogne.

To calculate the wave induced by wind stress, wind stress was parameterized as $\rho_a C_a U_{10}^2$ (ρ_a is air density (1 kg m^{-3}), C_a is the drag coefficient of air on the water surface and U_{10} is the 10-m wind speed). η_τ was then approximated by:

$$\eta_\tau \approx \frac{1}{2} \frac{\rho_a C_a U_{10}^2}{\rho g} \frac{x}{H_{Pr}}. \tag{7}$$

Inputting a 10 m s^{-1} 10-m wind speed, a drag coefficient of 0.0012 (Large and Pond 1981), and 37 m resonant water depth, then η_τ was about 0.03 m. If the wind stress and pressure components of the wave constructively interfered, then the maximum wave height after Proudman resonance would have been 0.34 m.

The maximum wave height at Boulogne was 0.70 m, meaning that 2.1 times more amplification would have been required. From the conservation of wave energy flux, waves grow when moving into shallower water as described by Green's Law (Pugh and Woodworth 2014):

$$\frac{\eta_1}{\eta_0} \propto \left(\frac{H_0}{H_1} \right)^{\frac{1}{4}}. \tag{8}$$

A wave with original wave height $\eta_0 = 0.34$ m, which was generated in depth $H_0 = H_{Pr} = 37$ m, and shoaled to depth $H_1 = 5$ m (approximate water depth at Boulogne in Figure 2), would have a resultant wave height $\eta_1 = 0.56$ m. The wave height may have then further amplified through refraction, but this is difficult to quantify without numerical modeling.

This analysis has provided some evidence towards the generation mechanisms of the observed wave. It has suggested that atmospheric pressure was the primary forcing (91%) and wind stress was secondary (9%), that external resonance occurred through Proudman resonance, and that shoaling produced further amplification. However, idealized analysis has only partly explained wave heights at Boulogne, rather than provide a deeper understanding of the link between generation mechanisms and the observed meteotsunami. Numerical models could provide this understanding, alongside stronger evidence for wave growth through Proudman resonance, and quantify wave height sensitivity to atmospheric forcing and tides.

3. Modeling

a. Telemac

We used the finite element ocean model Telemac (Hervouet 2000) to model the wave, which solved the two-dimensional non-linear shallow-water momentum and continuity equations. Here they are given in two-dimensional vector form:

$$\frac{\partial \mathbf{u}}{\partial t} + \mathbf{u}\cdot\nabla\mathbf{u} + \mathbf{f}\times\mathbf{u} = -g\nabla\eta - \frac{1}{\rho}\nabla p - \frac{g}{C^2}\frac{|\mathbf{u}|\,\mathbf{u}}{H+\eta} + C_a\frac{\rho_a}{\rho}\frac{|\mathbf{U_{10}}|\,\mathbf{U_{10}}}{H+\eta} + A_h\nabla^2\mathbf{u}\,, \tag{9}$$

$$\frac{\partial \eta}{\partial t} + \nabla\cdot\Big(\mathbf{u}(H+\eta)\Big) = 0\,, \tag{10}$$

where $\mathbf{u}$ is the depth-averaged horizontal velocity vector, ∇ is the horizontal gradient vector, t is time, C is the Chézy coefficient (60 $\mathrm{m}^{\frac{1}{2}}\ \mathrm{s}^{-1}$), A_h is the eddy viscosity (150 $\mathrm{m}^2\ \mathrm{s}^{-1}$), and $\mathbf{f}$ is the Coriolis parameter, directed vertically upward. With wind in the model, $\mathbf{U_{10}}$ is the 10-m wind vector.

Equations (9) and (10) were solved on a multi-scale triangular mesh, generated with Blue Kenue (Canadian Hydraulics Centre of the National Research Council Canada 2016), using 30 arc-second bathymetry from GEBCO 2014 (Ioc 2008). The mesh node spacing was 500 m in the eastern English Channel. For all non-tidal models, we used 2 second, fully-implicit time stepping and simulations ran for at least 22,000 seconds (6.1 hours).

b. Atmospheric forcing

The atmospheric pressure p was prescribed by an analytical forcing function:

$$p = \begin{cases} p_t \cdot \frac{\tanh \psi + 1}{2} \cdot \cos \phi + p_b & \text{if } -\frac{3\pi}{2} \leq \phi \leq \frac{3\pi}{2}; \\ p_b & \text{otherwise.} \end{cases} \tag{11}$$

The bounds of the argument $\phi = \mathbf{k} \cdot \mathbf{x} - \omega t$ describe a low–high–low pressure pattern, where $\mathbf{k}$ is the wave number vector, and $\mathbf{x}$ is the position vector. ω is angular frequency, where $\omega = 2\pi/T$ and T is the forcing period. The maximum pressure perturbation p_t was prescribed on a 1013 hPa background pressure p_b.

The geographical extent of the forcing was also parameterized, because the convective system did not extend to the UK, and could not be completely determined from the observations. The end of the convective system was determined as the last 20 mm h^{-1} precipitation-rate along the cross-propagation axis at multiple time steps. A linear regression through the end points was used as the extent of the modeled pressure anomaly (thick dashed line in Figure 3). In Equation 11, this was given by $\psi = \alpha(\Phi - 0.386\Lambda - 50.49^{\circ}N)$, where Φ = latitude, Λ = longitude and $\alpha = 1/4000$ m^{-1}.

The pressure perturbations were modeled using the best estimates provided by the observations, and ensembles were used to account for observational uncertainties. To create the ensemble, we

varied four characteristics: forcing speed U (17–22 m s^{-1}, 1 m s^{-1} increments), forcing direction θ (035–055°, 5° increments), pressure perturbation amplitude (0.9–1.5 hPa, 0.1 hPa increments) and forcing period (30–38 minutes, 1 minute increments). The model which we decided was the best estimate of atmospheric observations (not necessarily producing the most accurate wave height simulations) had 19 m s^{-1} forcing speed, 045° forcing direction, 1 hPa pressure perturbation amplitude, and 36 minute forcing period. The behavior in time for this case is shown in Figure 5, and contours of p can be seen in Figure 6.

c. Best-estimate model

A time series of the atmospheric pressure forcing with the best-estimate parameters is shown in Figure 5. The observed pressure anomaly was 10–60 minute bandpass filtered, removing the long-term synoptic signal and high-frequency noise. The model and observation timings were aligned such that the time of modeled high pressure perturbation coincided with the time of maximum pressure perturbation observed at Boulogne. At Le Touquet and Boulogne, the modeled and observed timings and pressure amplitudes were well represented. At Dunkirk, to the northeast, the modeled pressure was much lower amplitude and out of phase with observations. Also, at Le Havre the pressure anomaly was poorly approximated because the convective system approached from a different angle than was modeled. However, in the Proudman-resonant region there was good agreement between the model and the observed pressures, as well as the calculated velocities of radar-derived precipitation fields.

From the best-estimate model forcing, the sea surface height fields (Figure 6) show that two waves were initially created by the pressure system. The primary forced wave grew in the center of the English Channel (Figure 6a,b,c). There was also a coastal wave (dashed box in Figure 6b,c), which also grew as it propagated eastward along the French coastline to similar amplitudes

as the directly forced wave. At Dieppe it was this coastal wave that was recorded by the tide gage (Figure 7), which was followed by reflections from the French coastline. At Boulogne the directly forced wave arrived first, which was followed by the coastal wave up the French coastline and reflections from the UK coastline. At Le Havre the first wave to arrive was a directly forced wave underneath the pressure disturbance, and then reflections arrived later. At Newhaven the first wave to arrive was freely propagating away from the pressure disturbance. Reflections were also modeled from the French coastline back towards the UK (Figure 6d). In further analysis of the meteotsunami, different components of the wave are referred to as 'free', 'directly forced', 'coastal' and 'reflected'.

Examining the relationship between pressure disturbance and water level, the directly forced wave was proportional to the negative of the pressure gradient (compare pressure and sea level disturbance in Figure 6). This behavior is predicted by Equation 4, implying Proudman resonance. The directly forced wave also grew as it propagated along the Channel, in depths appropriate for Proudman resonance ($0.9 \leq \mathrm{Fr} \leq 1.1$). Using Equation 6, under perfect Proudman resonance, this wave should have grown by 0.10 m between 95–155 minutes. The model simulated 0.08 m wave growth over this time (0.12 m to 0.20 m). The directly forced wave grew within 20% of theoretical calculations of wave amplitude, consistent with the predictions of Proudman resonance. This is the strongest available evidence that this was the amplification mechanism for the directly forced wave.

This wave was not damaging, and compared to concurrent wind waves it had a similar wave energy flux density. When the wave uncoupled from the atmospheric forcing, the energy flux density of the directly forced wave was about 3.4 kW m^{-1}, which is similar to the energy flux density of 0.4-m high, 9-second period wind waves measured at the Greenwich Lightship Buoy (1.4 kW m^{-1}). However, meteotsunamis may be more damaging than this wave flux density

suggests. Long, coherent wave crests mean that a relatively large total energy flux is available for focussing. Here, 340 MW was available for focussing from the 100 km crest. Nonetheless, this meteotsunami was not damaging, and the simulations did not suggest considerable wave energy focussing through refraction in the English Channel.

The coastal wave growth was further investigated through idealized numerical models, because its growth mechanism was unclear and Greenspan resonance was previously discounted through Froude number arguments. In these models the bathymetry was assigned the previously approximated shallow and steep slopes near the French coastline, and a moving sinusoidal pressure forcing was prescribed (Figure 8). This idealized model reproduced the coastal wave under baseline slope approximations (Figure 8a). First we changed the gradient of the steep slope between 0.002 – 0.01, and a coastal wave with a similar amplitude to the forced wave was modeled (Figure 8e,f). The coastal wave was also reproduced when the pressure forcing was cut-off at $y = 6$ km, showing that it was not produced by direct forcing (Figure 8b). We then altered the shallow slope section such that Proudman resonance could not produce a large forced wave (Figure 8g). If the coastal wave were directly forced by the pressure disturbance over the steep slope, this should not affect the coastal wave amplitude. However, the coastal wave magnitude also decreased to the amplitude of the Proudman resonance forced wave. Therefore, the coastal wave was directly related to the forced wave generated in the English Channel by Proudman resonance and appeared to be separate because it was heavily refracted by the steep slope.

The arrival times and periods for both the coastal wave and directly forced wave were modeled well at Dieppe and Boulogne. The modeled arrival time at Boulogne, 0449, was only 2 minutes behind the observed arrival time, 0447 (Figure 7). The arrival time at Dieppe was more poorly recreated, which was measured as 0358 and modeled as 0405, a lag in the model of 7 minutes. The difference in arrival times between the waves at Boulogne and Dieppe gave a 5-minute relative

difference of modeled arrival times (44 minutes) compared to observations (49 minutes). The dominant period of the modeled wave is approximately 34–39 minutes at Boulogne and Dieppe, which is approximately 5 minutes longer than observed. The wave traveled faster in the model between Dieppe and Boulogne by a few minutes and the period of the wave was longer than expected.

The maximum wave heights, given by the maximum difference between consecutive peaks and troughs, were simulated to within tens of centimeters. At Boulogne, a 0.70 m wave was observed, compared to the best-estimate model 0.50 m wave height (29% underestimate). At Dieppe, a 0.43 m wave was observed, compared to the best-estimate model 0.33 m wave height (23% underestimate). The model did not produce a large wave at Le Havre but there were no discernible observations here either.

The model was poorer at representing sea surface elevation at Newhaven than at other locations. The best-estimate model produced a perturbation at Newhaven due to the initial movement of the convective system over the English Channel, which was not discernible in the observations. Also, the first peak of the reflected wave at Newhaven was about 30 minutes after the maximum observed peak, and the largest modeled peak was about 60 minutes after the maximum observed peak. However, the amplitudes of later perturbations were similar to observations (Figure 7). We accept the model limitations at Newhaven as the result of forcing simplifications, which did not include other storms that occurred prior to, and after, the synthetically modeled convective system (compare Figure 3 and Figure 6). These other storms could have produced forced waves (0.06 m high) that shoaled up to 0.10–0.14 m high at the Newhaven coastline (Fr $\sim$ 0.85, $H_0 \sim 50$ m, $H_1 \sim 1$ m, $\Delta P \sim \pm 0.75$ hPa, $\eta_0 = -\Delta P/\rho g(1 - Fr^2)$). Furthermore, the simplicity of the larger convective system would have affected both the initial free wave and the initial angles of freely

reflected waves at the French coastline (Vennell 2010). Nonetheless, it is difficult to compare the model output with sea surface observations sampled at 15-minute intervals.

d. Atmospheric forcing ensembles

To understand the sensitivities of the predictions of meteotsunami height and arrival times, we created ensembles by varying forcing velocity, amplitude of the pressure perturbations, and forcing period.

1) FORCING VELOCITY

Model results from forcing speeds at 17, 19 and 21 m s^{-1} across angles 035–055° are shown in Figure 9. The arrival time difference between the wave arriving in Boulogne and Dieppe was mostly dependent on the propagation time of the atmospheric forcing. The average of the relative differences in arrival times was 53 minutes, 42 minutes, 34 minutes at 17 m s^{-1}, 19 m s^{-1} and 21 m s^{-1} respectively. The faster the forcing speed, the smaller the modeled arrival time difference at each location. The relative arrival time of the wave was controlled by the forcing speed because the directly forced wave was trapped underneath the forcing. The modeled arrival time difference between Dieppe and Boulogne was 5 minutes too short, suggesting that the atmospheric system speed may have been slower than our best estimate, but falls within error estimates (19 $\pm$ 2 m s^{-1}).

Figure 9 shows that the modeled maximum wave heights varied with both forcing speeds and angles, but were mainly dependent on forcing speeds. Across 30 simulations, maximum wave heights at Boulogne were consistently obtained at 19 m s^{-1}, with greater than 0.4 m maximum wave heights averages obtained between 19–20 m s^{-1}. At Boulogne, wave height was relatively insensitive to forcing angle when the forcing speed was 19 m s^{-1}, ranging from 0.43–0.52 m

(0.48 m $\pm$ 9.5%); the largest wave heights were achieved at forcing angles between 040–050° and decreased away from these angles. Wave height was more sensitive to angle when the speed was 17 m s^{-1}, with maximum wave heights between 0.20–0.43 m (0.32 m $\pm$ 36%) at Boulogne. Dieppe was more sensitive to forcing angle than Boulogne, with maximum wave heights between 0.19–0.48 m (0.34 $\pm$ 44%) at 19 m s^{-1} and 0.29–0.59 m (0.44 m $\pm$ 34%) at 17 m s^{-1}. At Dieppe wave heights were largest at 055° and decreased with more northward forcing angles.

The wave height at Dieppe decreased as the forcing moved faster and more northward (Figure 9). Again, idealized models showed wave height sensitivity to forcing velocity; forcings moving towards the coastline produced larger waves (Figure 8c) and forcings moving away from the coastline produced smaller waves (Figure 8d). Also, because the Proudman resonant region was further from the coastline for faster forcings, smaller wave heights should be expected (Figure 8h).

Our sensitivity analysis in the English Channel also revealed that a forcing speed between 18–19 m s^{-1} would have improved arrival times, without degrading wave heights, at Boulogne and Dieppe (Figure 9i,j). The cause of arrival time error was probably because the atmospheric forcing velocity was treated as a constant velocity, whereas observations showed more complicated system movement (Figure 3). Nevertheless, the accuracy of modeled arrival times, period and wave height give confidence that the convective system moved at Proudman resonant velocity and produced the observed meteotsunami.

2) Pressure perturbation amplitude

Increasing the pressure perturbation amplitude increased the maximum wave height. A 0.9-hPa forcing produced a 0.45 m wave at Boulogne, and using a 1.5-hPa forcing produced a 0.74 m wave (Figure 10c,d). At Dieppe, a 0.9-hPa forcing produced a 0.30 m wave, and a 1.5-hPa forcing produced a 0.49 m wave. Linear regression of the maximum wave heights at Boulogne and Dieppe

from 0.9–1.5 hPa forcings, revealed a strongly linear relationship between pressure amplitude and maximum wave height. This linear relationship is a well-known result.

3) Forcing period

Changing the forcing period created more complicated resultant behavior in the modeled meteotsunami than altering the amplitude of the forcing (Figure 10e,f). There was some expected behavior in the absence of seiching. A longer period forcing generated a proportionally longer period meteotsunami, and all models with 30–38 minute period forcings agreed with the shape of the meteotsunami waveform at Dieppe. However, at Boulogne, modeled meteotsunami maximum wave heights behaved unpredictably after the first trough. Furthermore, the largest modeled wave was from the shortest period forcing at Boulogne, whereas at Dieppe the largest modeled wave was from the longest period forcing.

This sensitivity was from wave superposition of the direct forced wave at Boulogne and the coastal wave traveling up the coastline from Dieppe. From these results, hazard assessments should use various forcing periods.

e. Wind

When including wind, the 10-m wind velocity was modeled as two 10 m s^{-1} amplitude half-sinusoids with the same period as the pressure disturbance. The two wind maxima were aligned with where the pressure disturbance was 0 hPa, between the simulated mesohigh and mesolows, representing observations at Le Touquet (Figure 4). The wind vector field, which moved at the same velocity as p, was prescribed:

$$\mathbf{U_{10}} = U_{10}\cos\chi\,\hat{\mathbf{i}} + U_{10}\sin\chi\,\hat{\mathbf{j}}, \tag{12}$$

where $\chi = 45^\circ$ (northeastward 10-m winds), $\hat{\mathbf{i}}$ and $\hat{\mathbf{j}}$ were unit vectors in the eastward and northward directions respectively, and:

$$U_{10} = \begin{cases} |A \cdot \frac{\tanh \psi + 1}{2} \cdot \sin \phi| & \text{if } -\pi \leq \phi \leq \pi; \\ 0.01 & \text{otherwise,} \end{cases} \tag{13}$$

where A was 10 m s^{-1}, and all other variables were the same as for the pressure forcing.

The model locations corresponding to tide gages at Boulogne and Dieppe showed that wind changed the resultant maximum sea surface height by a few centimeters (Figure 10). The first peak of the wave increased at Boulogne from 0.24 m to 0.27 m (+13%). At Dieppe a similar increase is seen in the first peak, increasing from 0.14 m to 0.17 m (+21%). This was a 16% average increase in first peaks. The second wave peak was reduced by the wind by similar magnitudes; at Dieppe, the secondary peak decreased from 0.15 m to 0.14 m (–6.7%). Overall, the wind forcing was secondary to the pressure forcing for this meteotsunami.

The contribution from wind here was small compared to meteotsunamis generated by similar convective systems in the Great Lakes. Wind stress contribution can be large because of shallow water depths (Anderson et al. 2015), strong winds (Bechle and Wu 2014) or a combination of both factors (Šepić and Rabinovich 2014). Even with similar atmospheric forcings, wind stress and pressure disturbances may contribute different amounts to wave height between different basins due to basin bathymetry and geometry (Šepić and Rabinovich 2014). In Lake Erie, wind stress has accounted up to 59% of wave heights because of shallow average water depths (20 m), despite moderate observed wind speeds (10–15 m s^{-1}) (Anderson et al. 2015). In Lake Michigan, wind stress has contributed up to 40% of the wave height because of high 10-m wind speeds (25 m s^{-1}), despite deeper water (75–90 m) (Bechle and Wu 2014). Further analysis for the 23 June 2016 meteotsunami has suggested that if the 10-m wind speeds were larger (25 m s^{-1}) or the

Proudman-resonant water depths were shallower (20 m), wind stress would have contributed 30–50% of the wave height. The contribution of wind here was low (16%) because of low 10-m wind speeds and deep water.

f. Tides

Previous calculations (Section 2c) have shown that tides may have changed the location of Proudman resonance through local depth change and currents, which may have affected propagation speed and wave growth. Therefore, tides were included using boundary conditions from the TPXO European Shelf model. Tide was spun-up from a cold start from 0000 UTC 17 June 2016. A larger mesh with maximum 5-km node spacing extended the previous mesh across the western English Channel and above the southern North Sea amphidrome. Maximum modeled currents were ~ 3 m s^{-1} near Cherbourg and tidal ranges were about 10% smaller than observations, which were reasonable compared to other English Channel tidal models (Pingree and Maddock 1977; Davies 1986). It was not our intention to develop a precise tidal model, rather to adequately simulate tides to assess their influence.

Three simulations including tides were run, with high-pass filtered sea level results shown in Figure 11. With the best-estimate model forcing (U = 19 m s^{-1}, p_t = 1 hPa), the tidal model produced a 0.43 m maximum wave height at Boulogne, which was 0.07 m smaller than the non-tidal model (14% decrease); at Dieppe the tidal model wave height was 0.15 m, which was 0.18 m smaller than the non-tidal model (56% decrease). Reducing the atmospheric forcing speed to 18 m s^{-1} and increasing the pressure perturbation to 1.5 hPa produced a meteotsunami that was closer to observations and best-estimate results. The 18 m s^{-1}, 1.5 hPa, tidal model produced a 0.30 m maximum wave height at Dieppe, and 0.58 m maximum wave height at Boulogne. A model with U = 18 m s^{-1} and p_t = 1 hPa was also run (not shown), with maximum wave heights of 0.2 m at

Dieppe and 0.39 m at Boulogne. All tidal simulations produced small wave heights at Le Havre and Newhaven.

With tides included, the wave height changed at Dieppe because the Proudman resonant region shifted away from the coastline. In the numerical model, this occurred because southwestward tidal currents slowed the northeastward propagating meteotsunami by up to 1 m s^{-1} (about 5–6% decrease), and the tidal elevation lowered water levels by up to 0.5 m, reducing the meteotsunami wave speed by 0.1 m s^{-1} (about 0.5–0.6% decrease). Therefore, currents were mainly responsible for slowing the wave. Combined tidal effects reduced the shallow-water wave speed by 1.1 m s^{-1}, meaning that the Proudman resonant region shifted towards deeper water, farther from the coast. This partially explains how larger wave heights at Dieppe were reproduced when the forcing speed was decreased by 1 m s^{-1} — the Proudman resonant region moved nearer the coastline.

However, when forcing speed was decreased, increasing pressure amplitude by 1.5 times was required to simulate similar wave heights to the best-estimate model. This may be because of refraction of the wave due to currents offshore, leading to larger wave heights towards the center of the basin. The processes acting to decrease the coastal wave height were more important than steepening of the wave as it was moved against the current, leading to an overall decrease in wave height.

These simulations show that tides can change the location where Proudman resonance occurs, leading to a decrease of coastal wave height on the same order of magnitude as changing the atmospheric forcing parameters. Previous studies suggest that, even in macrotidal regimes, tides only change wave heights in open basins (i.e. no seiching) by 17% (Choi et al. 2014). This study shows that, even when tides are near still water level, tidal currents can considerably change the location of wave amplification and halve coastal wave heights.

Here, the best-estimate model under-predicted wave height even without tidal influence. Meteotsunamis are often difficult to simulate in both synthetic and NWP models (Anderson et al. 2015), particularly after the first peak (Choi et al. 2014), and across multiple locations (Hibiya and Kajiura 1982; Bechle and Wu 2014). Here, the tide reduced the meteotsunami wave height, decreasing the best-estimate wave height accuracy from 77% to 35% at Dieppe and from 71% to 61% at Boulogne. When the atmospheric forcing was altered within observational uncertainties, the wave height accuracy increased to 70% at Dieppe and to 83% at Boulogne, but the observed wave height was not fully resolved. These tidal results highlight the importance of accurately interpreting sparse observations, implementing accurate model forcings and accounting for observational uncertainty when modeling meteotsunamis.

4. Conclusions

We have combined observations and numerical models to show that meteotsunamis are generated in the English Channel by convective weather systems. We demonstrate for the first time in an English Channel case study that atmospheric pressure forcing, Proudman resonance, and shoaling were key amplification mechanisms. Wind stress was a secondary forcing and increased the first wave peak by 16% on average because of combined low wind speeds and deep water. Including tide in our model decreased the coastal wave height by more than 50%, mostly because tidal currents shifted the Proudman resonant region away from the coastline (rather than depth changes affecting the shallow water wave propagation speed directly).

The synthetic forcing simplicity may explain differences between best-estimate model results and observations. The best-estimate simulated arrival times and wave period within minutes and captured Proudman resonance, leading to estimates of wave heights accurate to within tens of centimeters (23–29% underestimates). Here, ensembles accounted for this uncertainty, testing

the sensitivity of the meteotsunami height to pressure perturbation amplitude, forcing velocity and forcing period. Nevertheless, considerable changes were found in wave height when testing sensitivity to each parameter. Wave height was linearly proportional to pressure amplitude, which is a well-known result. Forcing velocity and forcing period produced more complex changes in final wave height. Varying forcing speed between 17–19 m s^{-1} and forcing direction between 035–055° changed wave heights between 0.19–0.59 m at Dieppe and 0.20–0.52 m at Boulogne, by changing where wave amplification occurred through Proudman resonance. Changes in forcing period resulted in complex wave behavior after the primary peak, due to superposition of different components of the meteotsunami. We recommend that future studies use an ensemble approach including tides, and varying forcing period and forcing velocity.

This study has also shown, through models covering observational uncertainty, that cross-correlation of radar-derived precipitation is accurate enough to estimate atmospheric forcing velocity. Advantages of the cross-correlation method are that interpretations of gust fronts are not needed, estimates of velocity error are obtained, and the forcing velocity is calculated over water. It is also possible to calculate in near-real time in the UK given radar measurements every 5 minutes. To obtain accurate results from precipitation cross-correlation in convective systems, the effects of individual cell motion should be minimized by using longer time steps and rain-rate thresholds. Once these sources of error are addressed, cross-correlation of radar data is an accurate, simple method to calculate atmospheric system velocity.

Although atmospheric observations have both high temporal and spatial resolution, oceanographic observations could be improved with higher frequency observations at tide gages. Tide gages in the UK and elsewhere use long averaging periods to improve the accuracy of data for long-term sea-level studies. However, this hinders an improved understanding of potentially hazardous meteotsunamis where a shorter averaging period is recommended. It is also unclear how

sea level rise will affect future meteotsunami hazard. A small increase in the average sea level could decrease the return period of 1 in 100 year storm surges by 25–40 fold (Wahl 2017). If meteotsunamis also become more frequent (for example from increased convective activity in a warmer atmosphere), the ability to observe them will be fundamental to coastal protection. High frequency radar tide gages could be a solution; they are capable of measuring water level at 1-minute intervals, and are relatively cheap and easy to maintain (Woodworth and Smith 2003).

We have demonstrated that convective system-generated meteotsunamis can be simulated using simple synthetic models. This could lead to potentially useful hazard warning systems for north-western European seas, as has been conducted in the Adriatic (Šepić et al. 2015). We have also shown that meteotsunamis around the UK can be explained using dynamical arguments, and we have accurately simulated an observed meteotsunami by using sufficiently sampled pressure, wind and radar data.

Acknowledgments. David Williams is funded by the National Environmental Research Council's Understanding the Earth, Atmosphere and Ocean Doctoral Training Programme, Grant NE/L002469/1. We thank Lotfi Aouf from MétéoFrance for providing 1-minute atmospheric wind speed and pressure data, and two anonymous reviewers for their comments.

References

Anderson, E. J., A. J. Bechle, C. H. Wu, D. J. Schwab, G. E. Mann, and K. A. Lombardy, 2015: Reconstruction of a meteotsunami in Lake Erie on 27 May 2012: Roles of atmospheric conditions on hydrodynamic response in enclosed basins. *J. Geophys. Res. Oceans*, **120 (12)**, 8020–8038, doi:10.1002/2015JC010883.

606 Bechle, A. J., and C. H. Wu, 2014: The Lake Michigan meteotsunamis of 1954 revisited. *Nat.*
607 *Hazards*, **74 (1)**, 155–177.

608 Bechle, A. J., C. H. Wu, D. A. Kristovich, E. J. Anderson, D. J. Schwab, and A. B. Rabinovich,
609 2016: Meteotsunamis in the Laurentian Great Lakes. *Scientific Reports*, **6**, 37 832.

610 Belušić, D., and N. S. Mahović, 2009: Detecting and following atmospheric disturbances with a
611 potential to generate meteotsunamis in the Adriatic. *Phys. Chem. Earth*, **34 (17)**, 918–927.

612 Canadian Hydraulics Centre of the National Research Council Canada, 2016: Blue Kenue.
613 URL Available:http://www.nrccnrc.gc.ca/eng/solutions/advisory/blue_kenue_index.html., [On-
614 line; accessed 29-April-2016].

615 Choi, B. J., C. Hwang, and S. H. Lee, 2014: Meteotsunami tide interactions and high frequency
616 sea level oscillations in the eastern Yellow Sea. *J. Geophys. Res. Oceans*, **119 (10)**, 6725–6742,
617 doi:10.1002/2013JC009788.

618 Churchill, D. D., S. H. Houston, and N. A. Bond, 1995: The Daytona Beach wave of 3–4 July
619 1992: a shallow-water gravity wave forced by a propagating squall line. *Amer. Meteor. Soc.*,
620 **76 (1)**, 21–32.

621 Davies, A., 1986: A three-dimensional model of the Northwest European continental shelf, with
622 application to the M4 tide. *J. Phys. Oceanogr.*, **16 (5)**, 797–813.

623 Ewing, M., F. Press, and W. L. Donn, 1954: An Explanation of the Lake Michigan Wave of 26
624 June 1954. *Science*, **120 (3122)**, 684–686.

625 Frère, A., C. Daubord, A. Gailler, and H. Hébert, 2014: Sea level surges of June 2011 in the NE
626 Atlantic Ocean: observations and possible interpretation. *Meteorological Tsunamis: The US*
627 *East Coast and Other Coastal Regions*, Vol. 74, Springer, 179–196.

628 Greenspan, H. P., 1956: The generation of edge waves by moving pressure distributions. *J. Fluid*
629 *Mech.*, **1 (06)**, 574–592.

630 Haslett, S. K., H. E. Mellor, and E. A. Bryant, 2009: Meteo-tsunami hazard associated with sum-
631 mer thunderstorms in the United Kingdom. *Phys. Chem. Earth*, **34 (17)**, 1016–1022.

632 Hervouet, J.-M., 2000: TELEMAC modelling system: an overview. *Hydrol. Process*, **14 (13)**,
633 2209–2210.

634 Hibiya, T., and K. Kajiura, 1982: Origin of the Abiki phenomenon (a kind of seiche) in Nagasaki
635 Bay. *J. Meteor. Soc. Japan*, **38 (3)**, 172–182.

636 Ioc, I., 2008: BODC, 2003. Centenary Edition of the GEBCO Digital Atlas, published on CD-
637 ROM on behalf of the Intergovernmental Oceanographic Commission and the International
638 Hydrographic Organization as part of the General Bathymetric Chart of the Oceans. *British*
639 *oceanographic data centre, Liverpool*.

640 Kalnay, E., and Coauthors, 1996: The NCEP/NCAR 40-year reanalysis project. *Amer. Meteor.*
641 *Soc.*, **77 (3)**, 437–471.

642 Large, W., and S. Pond, 1981: Open ocean momentum flux measurements in moderate to strong
643 winds. *J. Phys. Oceanogr.*, **11 (3)**, 324–336.

644 Levin, B. W., and M. Nosov, 2009: *Physics of tsunamis*. Springer, 311–345 pp.

645 Ličer, M., B. Mourre, C. Troupin, A. Krietemeyer, A. Jansaá, and J. Tintoré, 2017: Numerical
646 study of the Balearic meteotsunami generation and propagation under synthetic gravity wave
647 forcing. *Ocean Model.*, **111**, 38–45.

Linares, A., and A. J. Bechle, 2018: Meteotusnami-induced rip currents on 4 July 2003 in Warren Dunes, Lake Michigan. Abstract presented at 2018 Ocean Sciences Meeting, Portland, OR, 12-16 Feb.

Markowski, P., and Y. Richardson, 2011: *Mesoscale meteorology in midlatitudes*, Vol. 2. John Wiley & Sons, 245–260 pp.

Met Office, 2003: Met Office Rain Radar Data from the NIMROD System, NCAS British Atmospheric Data Centre, 2017.

Monserrat, S., I. Vilibić, and A. Rabinovich, 2006: Meteotsunamis: atmospherically induced destructive ocean waves in the tsunami frequency band. *Nat. Hazards Earth Syst. Sci.*, **6 (6)**, 1035–1051.

Pingree, R., and L. Maddock, 1977: Tidal residuals in the English Channel. *J. Mar. Biol. Assoc. U. K.*, **57 (2)**, 339–354.

Proudman, J., 1929: The Effects on the Sea of Changes in Atmospheric Pressure. *Geophys. J. Int.*, **2 (4)**, 197–209.

Pugh, D., and P. Woodworth, 2014: *Sea-level science: understanding tides, surges, tsunamis and mean sea-level changes*. Cambridge University Press, 203 pp.

Rabinovich, A. B., and S. Monserrat, 1998: Generation of meteorological tsunamis (large amplitude seiches) near the Balearic and Kuril Islands. *Nat. Hazards*, **18 (1)**, 27–55.

Šepić, J., and A. B. Rabinovich, 2014: Meteotsunami in the Great Lakes and on the Atlantic coast of the United States generated by the "derecho" of June 29–30, 2012. *Meteorological Tsunamis: The US East Coast and Other Coastal Regions*, Springer, 75–107.

669 Šepić, J., I. Vilibić, and I. Fine, 2015: Northern Adriatic meteorological tsunamis: Assessment of
670 their potential through ocean modeling experiments. *J. Geophys. Res. Oceans*, **120 (4)**, 2993–
671 3010, doi:10.1002/2015JC010795.

672 Šepić, J., I. Vilibić, and N. S. Mahović, 2012: Northern Adriatic meteorological tsunamis:
673 observations, link to the atmosphere, and predictability. *J. Geophys. Res.*, **117 (C2)**, doi:
674 10.1029/2011JC007608.

675 Sheremet, A., U. Gravois, and V. Shrira, 2016: Observations of meteotsunami on the Louisana
676 shelf: a lone soliton with a soliton pack. *Nat. Hazards*, **84 (2)**, 471–492.

677 Sibley, A., D. Cox, D. Long, D. Tappin, and K. Horseburgh, 2016: Meteorologically generated
678 tsunami-like waves in the North Sea on 1/2 July 2015 and 28 May 2008. *Weather*, **71 (3)**, 68–74.

679 Tappin, D. R., A. Sibley, K. Horsburgh, C. Daubord, D. Cox, and D. Long, 2013: The English
680 Channel 'tsunami'of 27 June 2011: a probable meteorological source. *Weather*, **68 (6)**, 144–
681 152.

682 Vennell, R., 2010: Resonance and trapping of topographic transient ocean waves generated by a
683 moving atmospheric disturbance. *Journal of Fluid Mechanics*, **650**, 427–442.

684 Vilibić, I., 2008: Numerical simulations of the Proudman resonance. *Cont. Shelf Res.*, **28 (4)**,
685 574–581.

686 Vilibić, I., and J. Šepić, 2017: Global mapping of nonseismic sea level oscillations at tsunami
687 timescales. *Sci. Rep.*, **7**, 40 818.

688 Vilibić, I., J. Šepić, A. B. Rabinovich, and S. Monserrat, 2016: Modern approaches in meteot-
689 sunami research and early warning. *Front. Mar. Sci.*, **3**, 57.

690 Vučetić, T., I. Vilibić, S. Tinti, and A. Maramai, 2009: The Great Adriatic flood of 21 June 1978
691 revisited: An overview of the reports. *Phys. Chem. Earth*, **34 (17-18)**, 894–903.

692 Wahl, T., 2017: Sea-level rise and storm surges, relationship status: complicated! *Environ. Res.*
693 *Lett.*, **12 (11)**, 111 001.

694 Wertman, C. A., R. M. Yablonsky, Y. Shen, J. Merrill, C. R. Kincaid, and R. A. Pockalny, 2014:
695 Mesoscale convective system surface pressure anomalies responsible for meteotsunamis along
696 the US East Coast on June 13th, 2013. *Sci. Rep.*, **4**, 7143, doi:10.1038/srep07143.

697 Woodworth, P. L., and D. E. Smith, 2003: A one year comparison of radar and bubbler tide gauges
698 at Liverpool. *Int. Hydrogr. Rev.*, **4 (3)**, 42–49.

LIST OF FIGURES

Fig. 1. English Channel bathymetry (Ioc 2008) in filled contours from shallow (light blue) to deep (dark blue). The color saturates when bathymetry is deeper than 80 m. The black, hatched area is the still water level region where $0.9 \leq \mathrm{Fr} \leq 1.1$. The area bounded by white lines is the equivalent region with –0.5 m tidal elevation and –1 m s^{-1} current approximations. Tide gages locations have bold typeface, atmospheric stations have italic typeface and locations with both tide gages and atmospheric stations have italic bold typeface. The location names are abbreviated as: NH - Newhaven, LH - Le Havre, DP - Dieppe, LT - Le Touquet, BL - Boulogne, DK - Dunkirk, RB - Rouen Boos, EH - Evreux Huest, BT - Beauvais Tille, RO - Roissy, CR - Creil, PT - Pointoise, AG - Amiens Glisy, AB - Abbeville, ME - Meaulte, MV - Merville, CL - Calais, 1 - Paluel, 2 - Penly, 3 - Gravelines, 4 - Dungeness B, BUOY - Greenwich Lightship buoy. A 100 km scale is given. The model open boundaries are shown as a thin black lines. Land is shaded gray. Thick black lines are coastlines from the Basemap Python package. 35

Fig. 2. Left: Tide gage raw data, Right: High-pass filtered tide gage observations (< 2 hour periods) at (a, b) Boulogne (BL), (c, d) Dieppe (DP), (e, f) Le Havre (LH) and Newhaven (NH). The red box indicates meteotsunami arrival. Black dashed lines highlight missing data between 0527–0534 inclusive. 36

Fig. 3. Composite radar derived precipitation rates in mm h^{-1} are shown for 0220, 0320 and 0440 UTC 23 June 2016 in the English Channel (Met Office 2003). Thin black lines indicate where the Froude number is 0.9 and 1.1 with GEBCO 2014 bathymetry and a 19 m s^{-1} atmospheric system speed. The thick, dotted line is the calculated maximum horizontal extent of the convective system. Three gust fronts are indicated. Gust front 1 is long-dashed, gust front 2 is dot-dashed, and gust front 3 is dotted. In (d) the interpretation is shown. Yellow circles indicate a decaying cell, red circles indicate a strengthening cell. The arrowheads indicate the direction these cells moved between 0315–0325 UTC. The gust fronts are shown in cyan. Locations of atmospheric stations at Le Havre (LH), Dieppe (DP), Le Touquet (LT) and Boulogne (BL) are shown. A 100 km scale is given. Land is shaded gray. Thick black lines are coastlines from the Basemap Python package. 37

Fig. 4. High-pass filtered atmospheric observations at Dieppe (purple), Le Touquet (red), Boulogne (cyan), Calais (green) and Dunkirk (blue). Top: 2-hour cut-off high-pass filtered air pressure time series. Bottom: Average 10-m wind speed over 10-minute windows. Pressure and wind speed sampled once per minute. 38

Fig. 5. Red - modeled pressure anomaly/ hPa for the model U = 19 m s^{-1}, $\theta = 045°$, $T = 36$ minutes, $p_t = 1$ hPa. Blue - 10–60 minute bandpass filtered pressure/ hPa. Top to bottom: Dunkirk, Boulogne, Le Touquet, Le Havre. 39

Fig. 6. Modeled sea level elevation (colors) at (a) 95, (b) 155, (c) 215 and (d) 315 minutes into the best-estimate simulation. Froude number contours at 0.9 and 1.1 from unaltered GEBCO bathymetry are shown as thin black lines. The western open boundary is shown in black. The sea level pressure is shown in black solid (+0.5 hPa) and dashed (–0.5 hPa) lines. All panels give interpretation of the modeled sea level elevation, with the coastal wave in a dashed black box in (b) and (c). The 21-m isobath is shown as a thin white line. Note the color saturates at +0.2 m and –0.2 m. 40

Fig. 7. Red - modeled sea surface elevation at tide gages for the model $U = 19$ m s^{-1}, $\theta = 045°$, $T =$ 36 minutes, $p_t = 1$ hPa. Blue - 10–60 minute bandpass filtered observations. Top to bottom: Boulogne, Dieppe, Le Havre, Newhaven. 41

Fig. 8. Idealized simulations investigating coastal wave generation mechanism. Colors range from –0.1 to +0.1 m. Black contours are +0.5 hPa and –0.5 hPa pressure anomalies. (a) Base line model. Infinite cross-propagation length, U = 17 m s^{-1}, normal bathymetry $\beta_0 = 0.0035, \beta_1 = 0.00037$, (b) Pressure cut off in the cross propagation direction at 6 km (dot-dashed black line). (c) moving towards the coastline, (d) moving away from coastline, (e) steep slope made steeper ($\beta_0 = 0.01$), (f) steep slope made shallower ($\beta_0 = 0.002$), (g) shallow slope between 6–60 km made flat ($\beta_1 = 0$), (h) forcing speed is 18 m s^{-1}. 42

Fig. 9. Sea surface elevation sensitivity to forcing angles and speeds. Model runs at each angle (035–055°) are shown in (a, b) at 17 m s^{-1} in purple, in (c, d) at 19 m s^{-1} in red, and in (e, f) at 21 m s^{-1} in cyan. On the left are the model results from Dieppe, and on the right from Boulogne. Each individual colored line in panels (a–f) represent an individual simulation at a specific forcing speed and angle. The solid black line is the mean across individual models, and the dashed black line are one standard deviation from the mean. Panels (g) and (h) compare the averages and standard deviations from 17 m s^{-1}, 19 m s^{-1} and 21 m s^{-1} at Dieppe and Boulogne in respective colors. Panels (i) and (j) compare the averages from each speed with the bandpass filtered observations in gray. In (i) and (j), simulation timings and observation timings are aligned with respect to the average of U = 19 m s^{-1} simulations. Note the change in scale and time shift in (i) and (j). 43

Fig. 10. Sea surface elevation sensitivity to wind, amplitude and period. Left is Dieppe, right is Boulogne. (a, b) 10 m s^{-1} wind component on (solid line) and off (dashed) where U = 19 m s^{-1}, θ = 045°, T = 36 mins and p_t = 1 hPa. (c, d) varying p_t between 0.9 hPa (blue), 1.2 hPa (red) and 1.5 hPa (cyan) where U = 19 m s^{-1}, θ = 045° and T = 36 mins. (e, f) varying T between 30 mins (blue), 34 mins (red) and 38 mins (cyan) where U = 19 m s^{-1}, θ = 045° and p_t = 1 hPa. Note the change in y-axis scale for (c) and (d). 44

Fig. 11. Sensitivity of the meteotsunami to tides in the model. (a) Boulogne, (b) Dieppe. Blue - 10–60 minute bandpass filtered observations. Red solid line - forcing model U = 19 m s^{-1}, θ = 045°, T = 36 minutes, p_t = 1 hPa without tides. Red dashed line - same atmospheric forcing as red solid line, but with tides. Black dash-dot line - for the model U = 18 m s^{-1}, θ = 045°, T = 36 minutes, p_t = 1.5 hPa with tides. 45

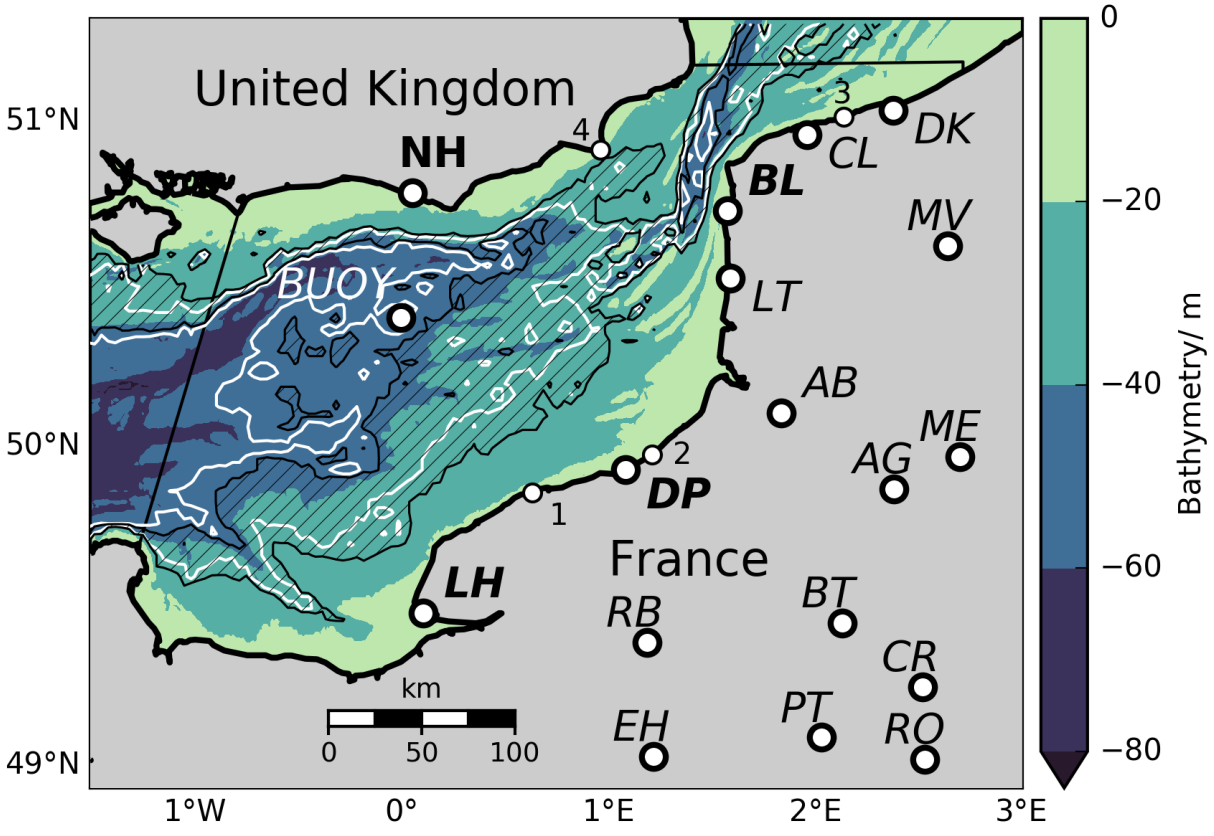

774 FIG. 1. English Channel bathymetry (Ioc 2008) in filled contours from shallow (light blue) to deep (dark
775 blue). The color saturates when bathymetry is deeper than 80 m. The black, hatched area is the still water
776 level region where $0.9 \leq \mathrm{Fr} \leq 1.1$. The area bounded by white lines is the equivalent region with –0.5 m tidal
777 elevation and –1 m s^{-1} current approximations. Tide gages locations have bold typeface, atmospheric stations
778 have italic typeface and locations with both tide gages and atmospheric stations have italic bold typeface. The
779 location names are abbreviated as: NH - Newhaven, LH - Le Havre, DP - Dieppe, LT - Le Touquet, BL -
780 Boulogne, DK - Dunkirk, RB - Rouen Boos, EH - Evreux Huest, BT - Beauvais Tille, RO - Roissy, CR - Creil,
781 PT - Pointoise, AG - Amiens Glisy, AB - Abbeville, ME - Meaulte, MV - Merville, CL - Calais, 1 - Paluel, 2
782 - Penly, 3 - Gravelines, 4 - Dungeness B, BUOY - Greenwich Lightship buoy. A 100 km scale is given. The
783 model open boundaries are shown as a thin black lines. Land is shaded gray. Thick black lines are coastlines
784 from the Basemap Python package.

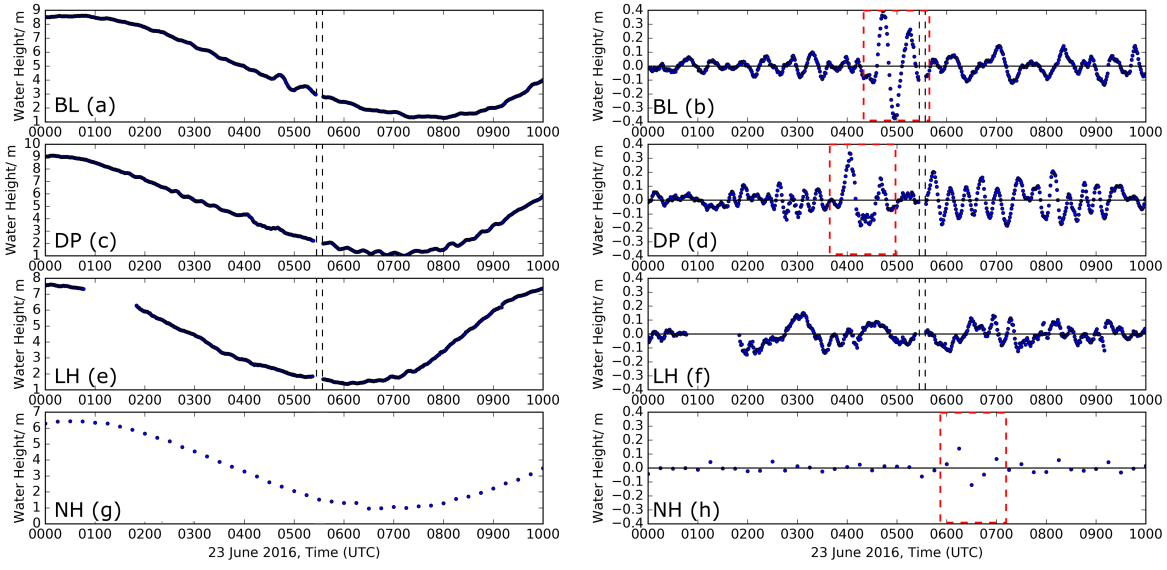

785 FIG. 2. Left: Tide gage raw data, Right: High-pass filtered tide gage observations (< 2 hour periods) at
786 (a, b) Boulogne (BL), (c, d) Dieppe (DP), (e, f) Le Havre (LH) and Newhaven (NH). The red box indicates
787 meteotsunami arrival. Black dashed lines highlight missing data between 0527–0534 inclusive.

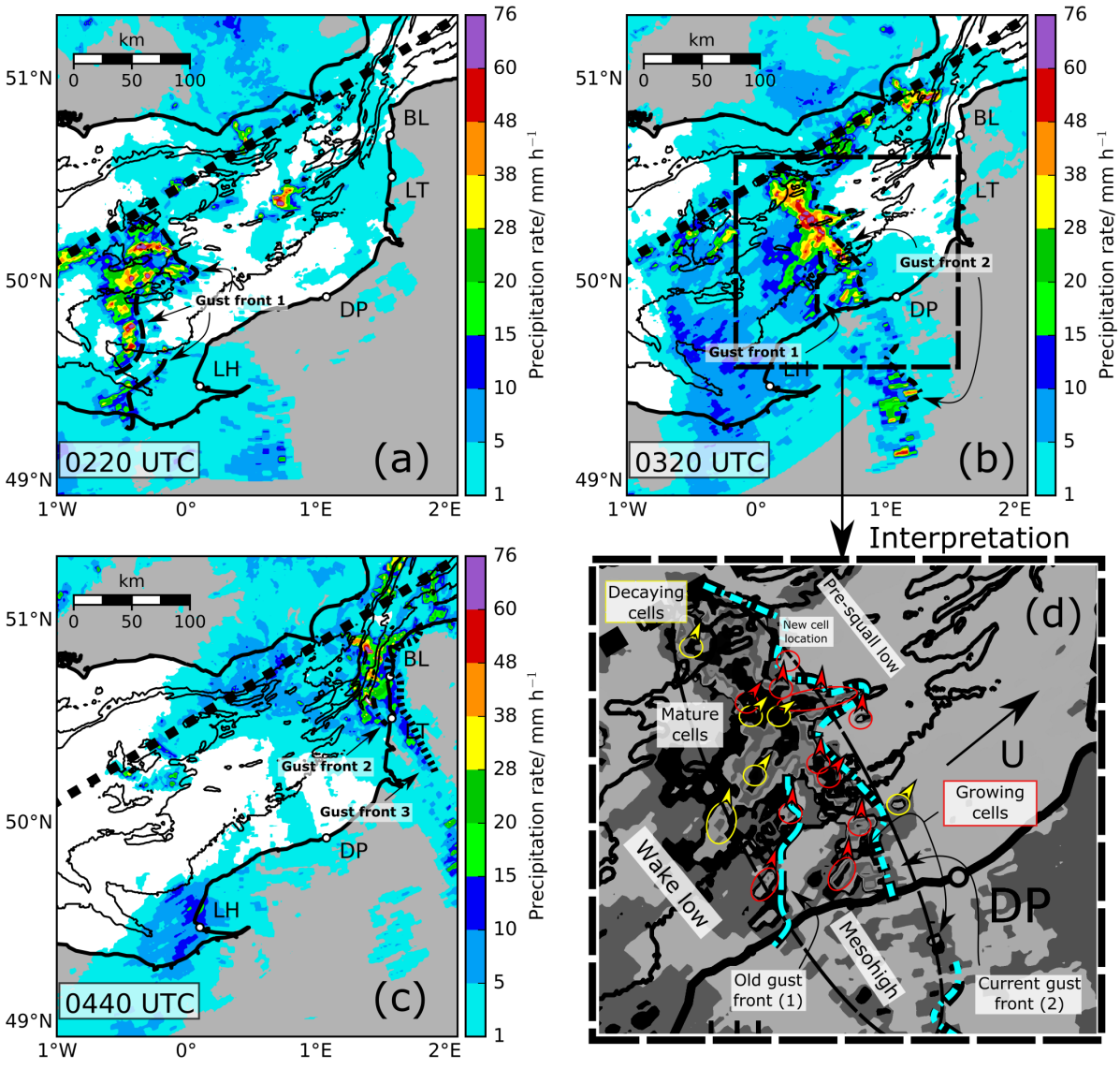

788 FIG. 3. Composite radar derived precipitation rates in mm h^{-1} are shown for 0220, 0320 and 0440 UTC 23
789 June 2016 in the English Channel (Met Office 2003). Thin black lines indicate where the Froude number is 0.9
790 and 1.1 with GEBCO 2014 bathymetry and a 19 m s^{-1} atmospheric system speed. The thick, dotted line is the
791 calculated maximum horizontal extent of the convective system. Three gust fronts are indicated. Gust front 1
792 is long-dashed, gust front 2 is dot-dashed, and gust front 3 is dotted. In (d) the interpretation is shown. Yellow
793 circles indicate a decaying cell, red circles indicate a strengthening cell. The arrowheads indicate the direction
794 these cells moved between 0315–0325 UTC. The gust fronts are shown in cyan. Locations of atmospheric
795 stations at Le Havre (LH), Dieppe (DP), Le Touquet (LT) and Boulogne (BL) are shown. A 100 km scale is
796 given. Land is shaded gray. Thick black lines are coastlines from the Basemap Python package.

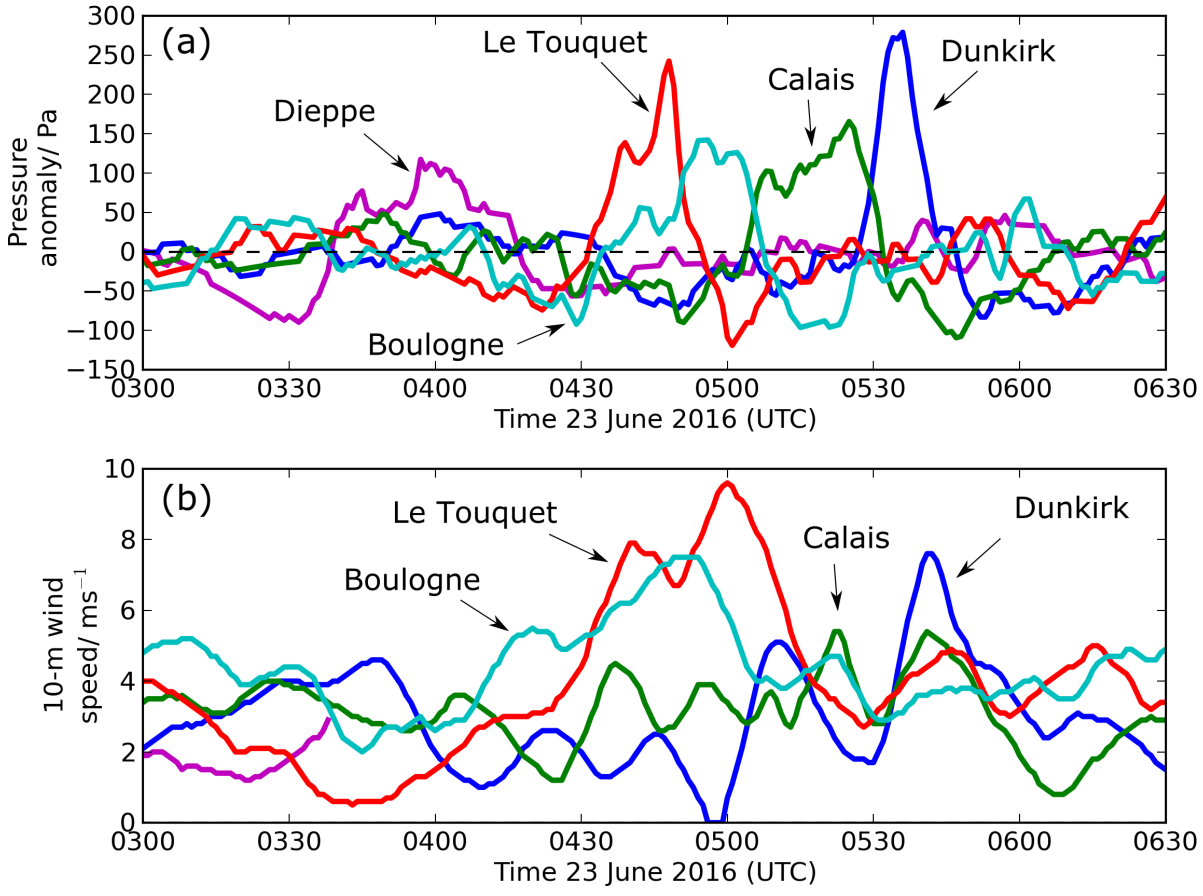

797 FIG. 4. High-pass filtered atmospheric observations at Dieppe (purple), Le Touquet (red), Boulogne (cyan),
798 Calais (green) and Dunkirk (blue). Top: 2-hour cut-off high-pass filtered air pressure time series. Bottom:
799 Average 10-m wind speed over 10-minute windows. Pressure and wind speed sampled once per minute.

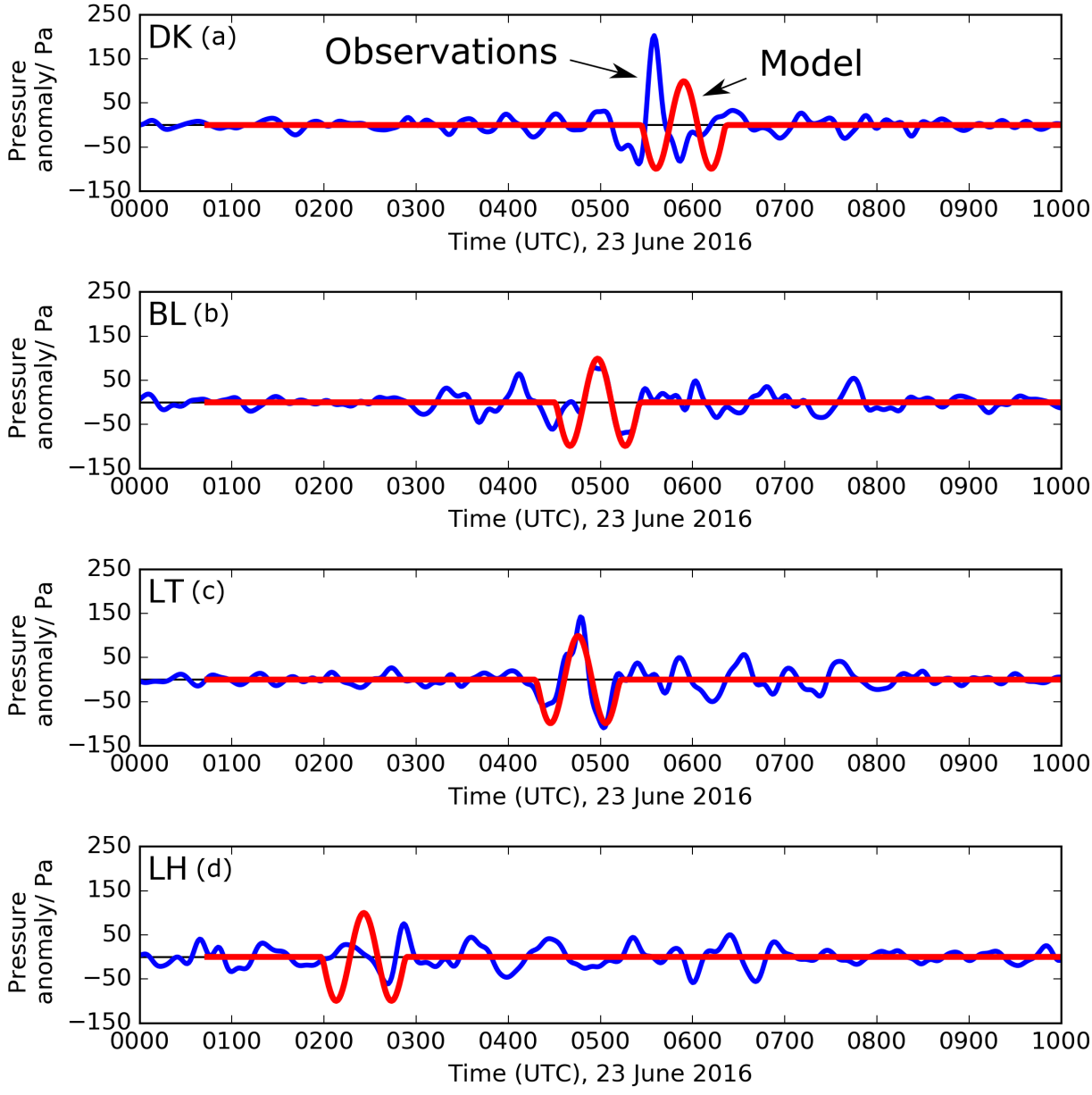

800 FIG. 5. Red - modeled pressure anomaly/ hPa for the model U = 19 m s^{-1}, $\theta = 045°$, $T = 36$ minutes, $p_t = 1$
801 hPa. Blue - 10–60 minute bandpass filtered pressure/ hPa. Top to bottom: Dunkirk, Boulogne, Le Touquet, Le
802 Havre.

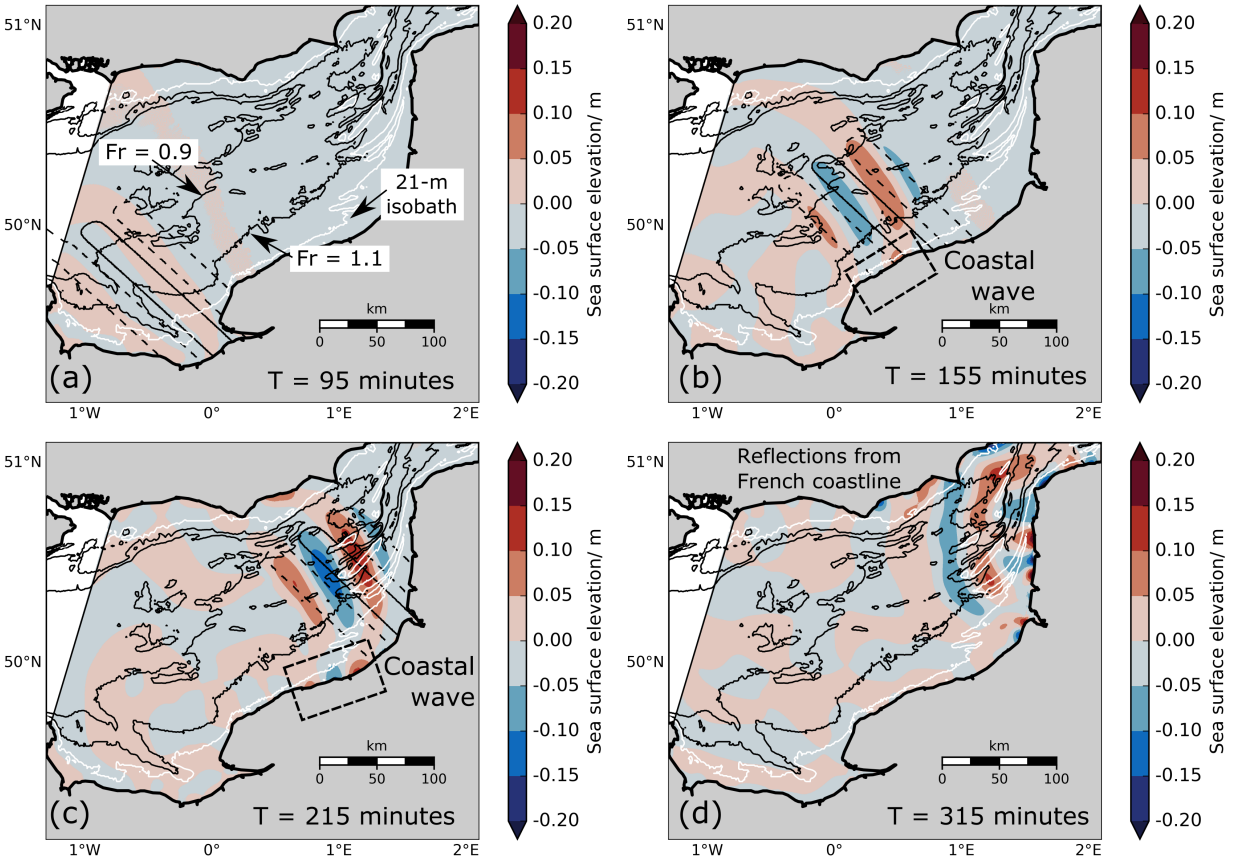

FIG. 6. Modeled sea level elevation (colors) at (a) 95, (b) 155, (c) 215 and (d) 315 minutes into the best-estimate simulation. Froude number contours at 0.9 and 1.1 from unaltered GEBCO bathymetry are shown as thin black lines. The western open boundary is shown in black. The sea level pressure is shown in black solid (+0.5 hPa) and dashed (–0.5 hPa) lines. All panels give interpretation of the modeled sea level elevation, with the coastal wave in a dashed black box in (b) and (c). The 21-m isobath is shown as a thin white line. Note the color saturates at +0.2 m and –0.2 m.

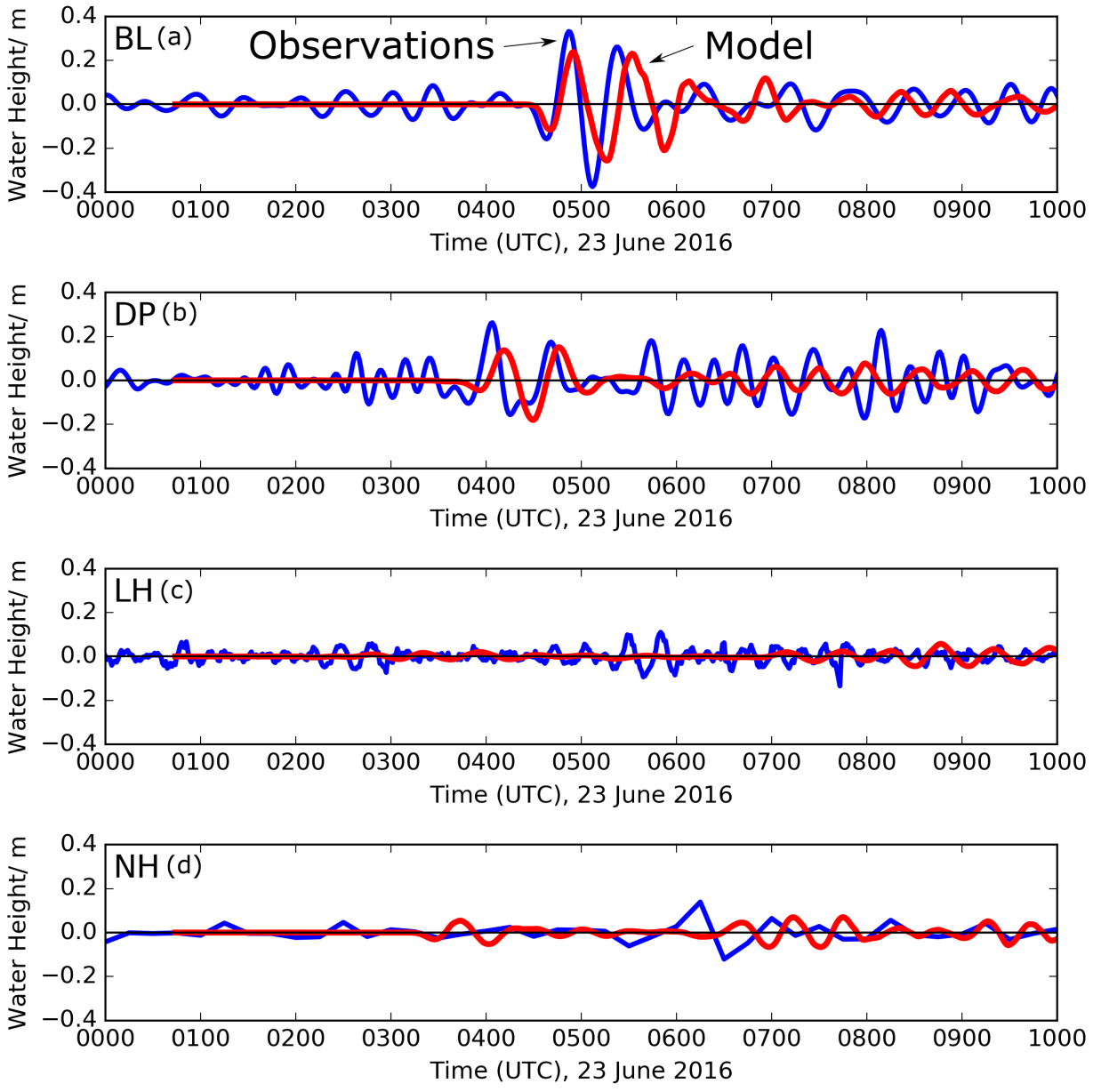

809 FIG. 7. Red - modeled sea surface elevation at tide gages for the model U = 19 m s^{-1}, θ = 045°, T = 36
810 minutes, p_t = 1 hPa. Blue - 10–60 minute bandpass filtered observations. Top to bottom: Boulogne, Dieppe, Le
811 Havre, Newhaven.

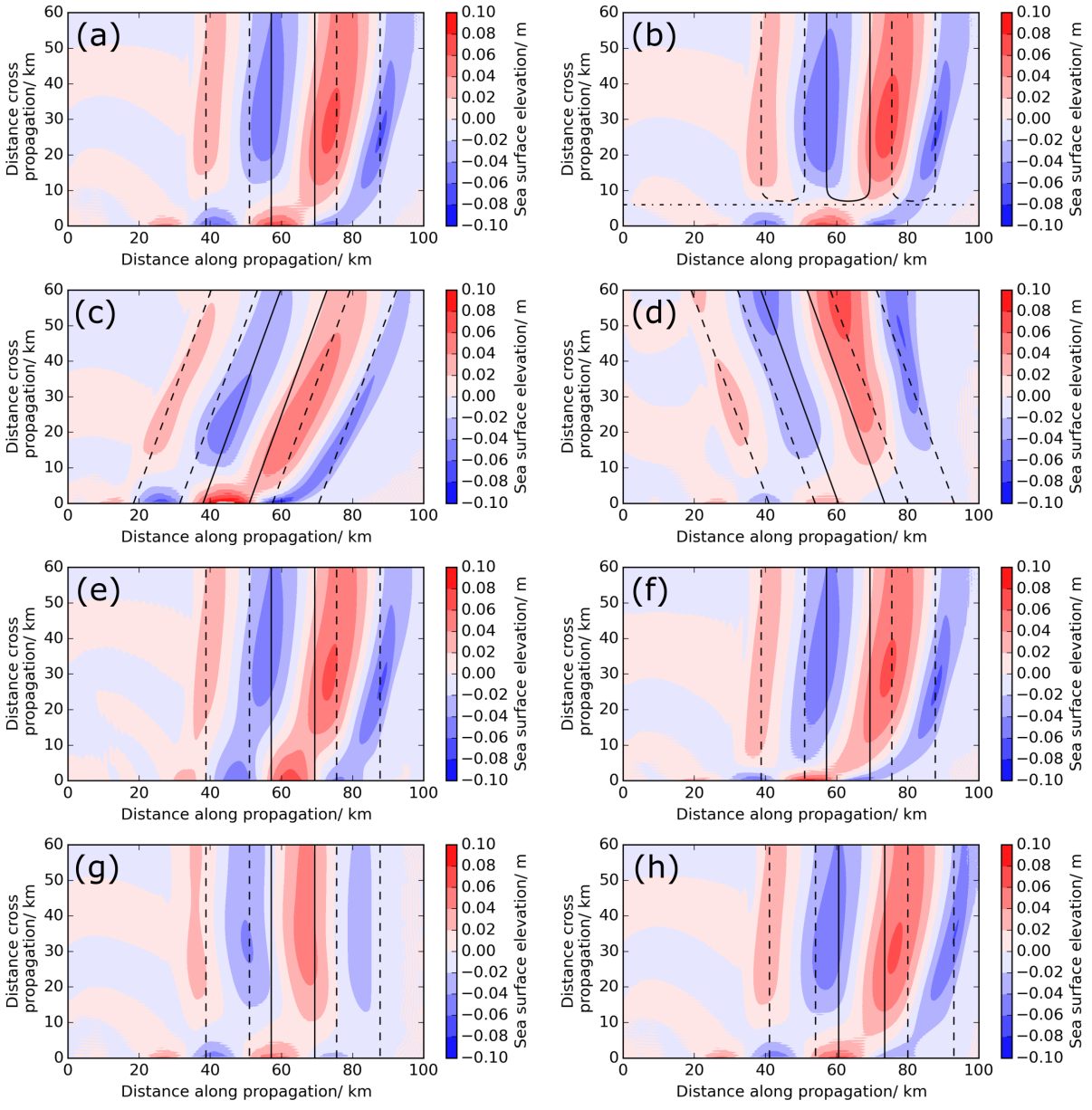

812 FIG. 8. Idealized simulations investigating coastal wave generation mechanism. Colors range from –0.1 to
813 +0.1 m. Black contours are +0.5 hPa and –0.5 hPa pressure anomalies. (a) Base line model. Infinite cross-
814 propagation length, U = 17 m s^{-1}, normal bathymetry $\beta_0 = 0.0035, \beta_1 = 0.00037$, (b) Pressure cut off in the
815 cross propagation direction at 6 km (dot-dashed black line). (c) moving towards the coastline, (d) moving away
816 from coastline, (e) steep slope made steeper ($\beta_0 = 0.01$), (f) steep slope made shallower ($\beta_0 = 0.002$), (g) shallow
817 slope between 6–60 km made flat ($\beta_1 = 0$), (h) forcing speed is 18 m s^{-1}.

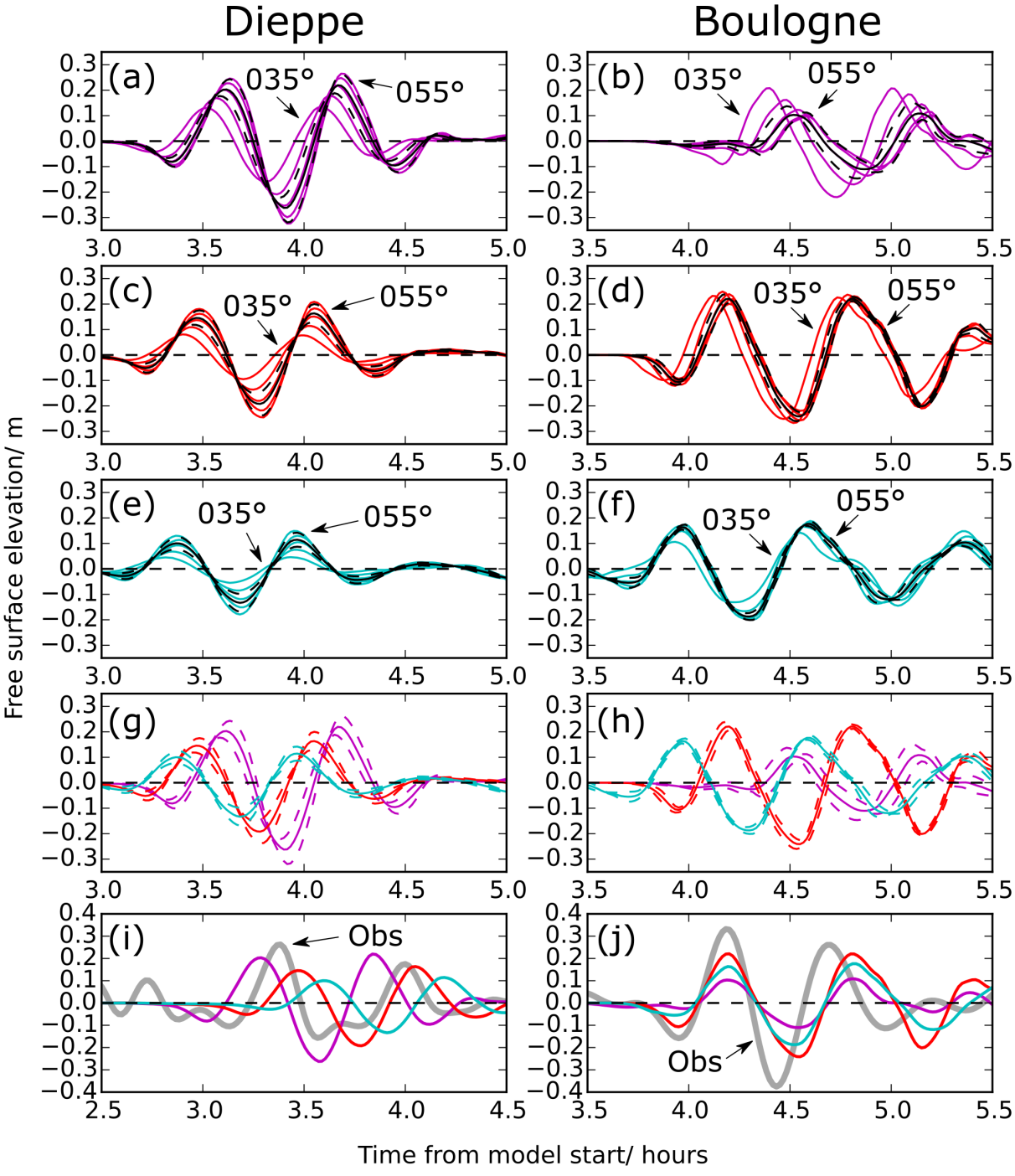

818 FIG. 9. Sea surface elevation sensitivity to forcing angles and speeds. Model runs at each angle (035–055°)
819 are shown in (a, b) at 17 m s^{-1} in purple, in (c, d) at 19 m s^{-1} in red, and in (e, f) at 21 m s^{-1} in cyan. On
820 the left are the model results from Dieppe, and on the right from Boulogne. Each individual colored line in
821 panels (a–f) represent an individual simulation at a specific forcing speed and angle. The solid black line is the
822 mean across individual models, and the dashed black line are one standard deviation from the mean. Panels
823 (g) and (h) compare the averages and standard deviations from 17 m s^{-1}, 19 m s^{-1} and 21 m s^{-1} at Dieppe
824 and Boulogne in respective colors. Panels (i) and (j) compare the averages from each speed with the bandpass

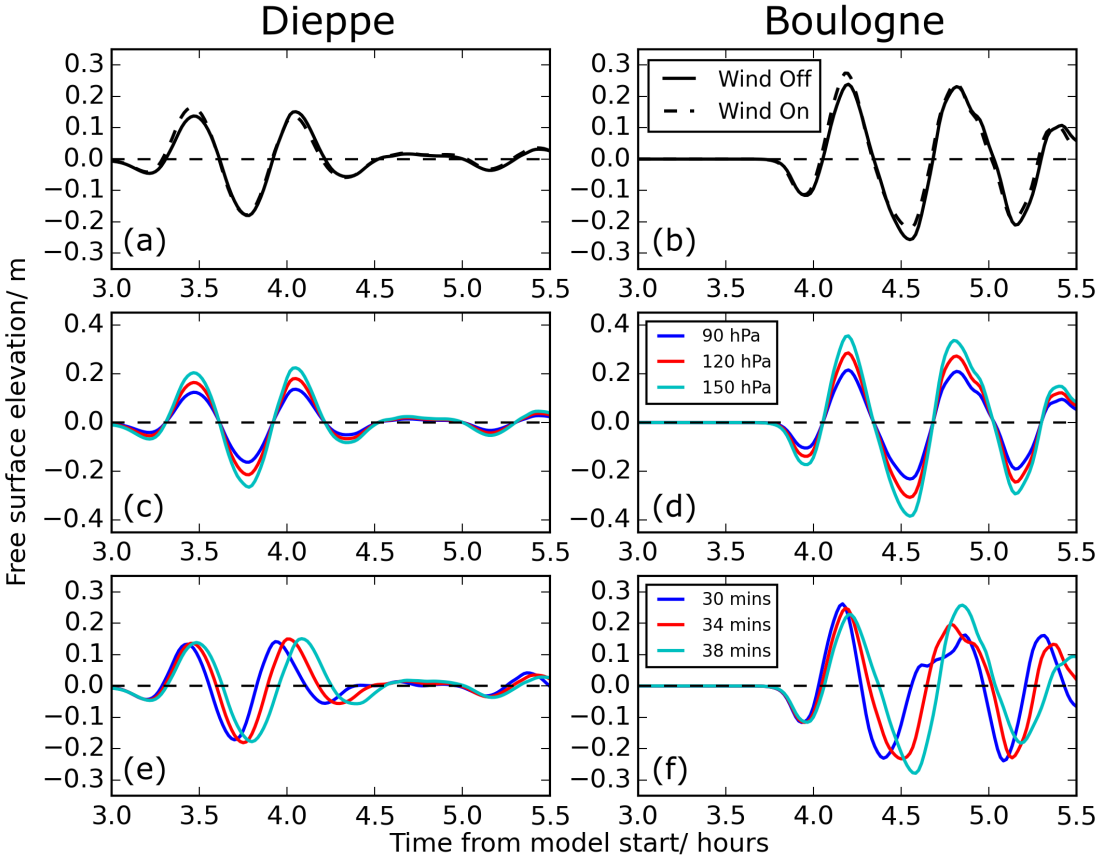

827 FIG. 10. Sea surface elevation sensitivity to wind, amplitude and period. Left is Dieppe, right is Boulogne.
828 (a, b) 10 m s^{-1} wind component on (solid line) and off (dashed) where U = 19 m s^{-1}, θ = 045°, T = 36 mins
829 and p_t = 1 hPa. (c, d) varying p_t between 0.9 hPa (blue), 1.2 hPa (red) and 1.5 hPa (cyan) where U = 19 m s^{-1},
830 θ = 045° and T = 36 mins. (e, f) varying T between 30 mins (blue), 34 mins (red) and 38 mins (cyan) where U
831 = 19 m s^{-1}, θ = 045° and p_t = 1 hPa. Note the change in y-axis scale for (c) and (d).

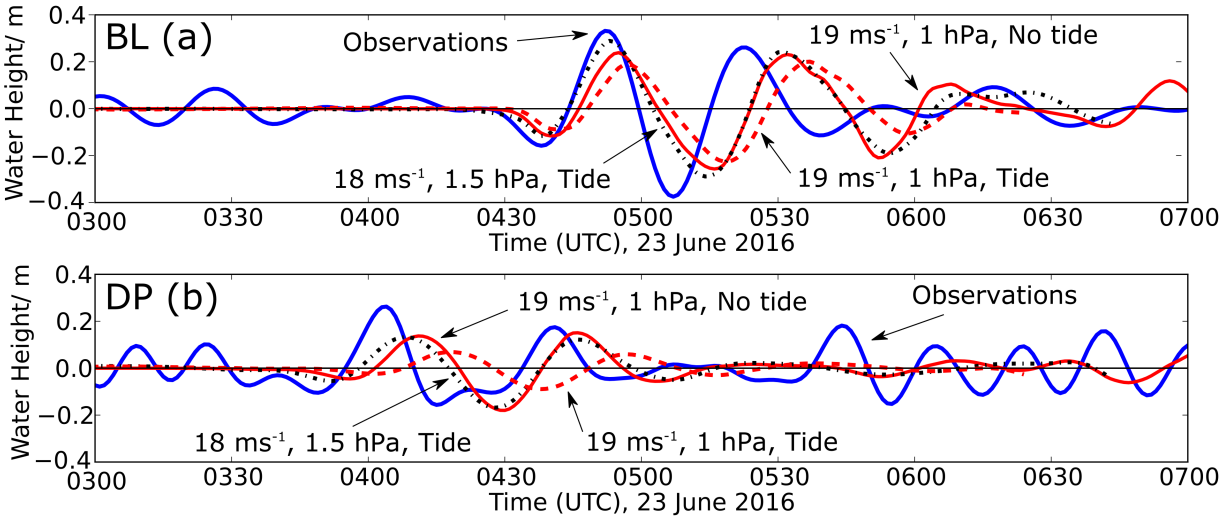

832 FIG. 11. Sensitivity of the meteotsunami to tides in the model. (a) Boulogne, (b) Dieppe. Blue - 10–60 minute
833 bandpass filtered observations. Red solid line - forcing model $U = 19$ m s^{-1}, $\theta = 045°$, $T = 36$ minutes, $p_t = 1$
834 hPa without tides. Red dashed line - same atmospheric forcing as red solid line, but with tides. Black dash-dot
835 line - for the model $U = 18$ m s^{-1}, $\theta = 045°$, $T = 36$ minutes, $p_t = 1.5$ hPa with tides.